



## Impact of Increasing Horizontal and Vertical Resolution during the HWRF Hybrid EnVar Data Assimilation on the Analysis and Prediction of Hurricane Patricia (2015)

JIE FENG<sup>a</sup> AND XUGUANG WANG<sup>a</sup>

<sup>a</sup>*School of Meteorology, University of Oklahoma, Norman, Oklahoma*

(Manuscript received 8 May 2020, in final form 13 November 2020)

**ABSTRACT:** Although numerous studies have demonstrated that increasing model spatial resolution in free forecasts can potentially improve tropical cyclone (TC) intensity forecasts, studies on the impact of model resolution during data assimilation (DA) on TC prediction are lacking. In this study, using the ensemble-variational DA system for the Hurricane Weather Research and Forecasting (HWRF) Model, we investigated the individual impact of increasing the model resolution of first guess (FG) and background ensemble (BE) forecasts during DA on initial analyses and subsequent forecasts of Hurricane Patricia (2015). The impacts were compared between horizontal and vertical resolutions and also between the tropical storm (TS) and hurricane assimilation during Patricia. The results show that increasing the horizontal or vertical resolution in FG has a larger impact than increasing the resolution in BE on improving the analyzed TC intensity and structure for the hurricane stage. The result is reversed for the TS stage. These results are attributed to the effectiveness of increasing the FG resolution in intensifying the background vortex for the hurricane stage relative to the TS stage. Increasing the BE resolution contributes to improving the analyzed intensity through the better-resolved background correlation structure for both the hurricane and TS stages. Increasing horizontal resolution has an overall larger effect than increasing vertical resolution in improving the analysis at the hurricane stage and their effects are close for the analysis at the TS stage. Additionally, the more accurately analyzed primary circulation, secondary circulation, and warm-core structures via the increased resolution in DA lead to improved TC intensity forecasts.

**KEYWORDS:** Hurricanes; Kalman filters; Numerical weather prediction/forecasting; Data assimilation; Ensembles

### 1. Introduction

Over the past few decades, great efforts have been made to improve the accuracy of tropical cyclone (TC) forecasts. The major endeavors include the development of high-resolution cloud-resolving numerical weather prediction (NWP) models, advanced data assimilation (DA) systems, and novel observing systems for TCs. So far, the accuracy of TC analysis and prediction has been steadily and significantly improved. For example, the yearly averaged track forecast at the 5-day lead time for the Atlantic basin in 2016 has a smaller error than the forecast at the 2-day lead time in 1990 (Katz and Murphy 2015).

Despite the substantial improvement in TC track forecasts, the progress in TC intensity forecasts is relatively limited (Harnos and Nesbitt 2011; DeMaria et al. 2014). Various studies have reported that the accuracy of TC intensity forecasts for the past few decades has little or even no improvements (e.g., Harnos and Nesbitt 2011; Zhang and Tao 2013). Current operational forecasts initialized using state-of-the-art hurricane analysis/prediction systems to assimilate the novel TC observations often fail to capture the TC rapid intensification (RI) process and the maximum intensity, particularly for strong hurricanes. For example, for the record-breaking intense (category 5) and extraordinarily small Hurricane Patricia

in 2015, none of the main operational dynamical and statistical-dynamical models even predicted a maximum intensity forecast above category 2 (Rogers et al. 2017).

Many previous studies in the literature have demonstrated that simply increasing the model horizontal or vertical resolution during the free numerical integration can effectively improve TC intensity forecasts. For example, some studies based on a large number of cases suggested the increase of model horizontal resolution has positive impacts on the accuracy of both TC track (Zhang et al. 2011; Davis et al. 2010; Gopalakrishnan et al. 2012) and intensity (Zhang et al. 2011; Gopalakrishnan et al. 2012) forecasts. Similar conclusions were also drawn in numerous case studies (e.g., Chen et al. 2007; Qin and Zhang 2018; Lu and Wang 2019; Feng and Wang 2019; Nystrom and Zhang 2019). In addition to the horizontal resolution, increasing the model vertical resolution during the numerical integration is also found to have a nonnegligible positive impact on the TC track (e.g., Zhang et al. 2016) and intensity (e.g., Zhang and Wang 2003; Kimball and Dougherty 2006; Zhang et al. 2015) predictions. These studies generally concluded that the improved TC intensity and structure forecasts mainly stem from the more realistic depiction of the TC finescale kinematic and thermodynamic structure and evolution due to the increase of model resolution. However, most of these studies are solely focused on the effect of model resolution during free forecasts by simply interpolating the initial analysis to higher resolution before initializing the numerical

Corresponding author: Xuguang Wang, xuguang.wang@ou.edu

model. Moreover, the comparison between the impacts from horizontal and vertical resolution is lacking in most of these studies.

The development of novel observing techniques has significantly improved the capability of observing hurricanes. In particular, tail Doppler radar (TDR) and dropsonde observations onboard reconnaissance aircraft are able to capture the detailed TC inner core structure and dynamic process. The assimilation of these new observations in advanced DA systems also greatly enhanced the accuracy of TC initial analyses and subsequent forecasts (e.g., Zhang et al. 2009; Pu et al. 2009; Li et al. 2012; Lu et al. 2017a; Feng and Wang 2019). Nevertheless, considerable TC intensity errors still exist at the early forecast lead times even using advanced DA systems based on cloud-resolving NWP models such as the ensemble-based DA for Weather Research and Forecasting (WRF) (e.g., Weng and Zhang 2012; Sippel et al. 2014; Christoffersen et al. 2017) and Hurricane WRF (HWRF; e.g., Tong et al. 2018; Lu and Wang 2019). As hypothesized by Lu and Wang (2019), the analyses from advanced DA systems may still not be able to resolve the finescale TC structure and dynamics as a result of insufficient model resolution adopted during the data assimilation. In particular, for an ensemble-based DA system, insufficient model resolution can degrade both the deterministic first guess (FG) and the background ensemble (BE) covariance and thus decrease the accuracy of TC analyses.

Unlike earlier studies, this paper aims to investigate how increasing the model resolution of FG and BE *during data assimilation* affects the analysis and prediction of TC intensity and structure. In particular, the impacts of both the horizontal and vertical resolution are studied and compared. The impacts are also investigated for different initial TC phases (i.e., tropical storm and hurricane). Diagnostics are performed to understand how the differences of analyses as a result of different model resolutions influence the subsequent intensity and structure predictions.

Hurricane Patricia (2015) is selected for this study. The choice of this case is inspired by our recent studies (Fig. 5 in Lu and Wang 2019; Fig. 2 in Feng and Wang 2019) in which the analyzed intensity of Hurricane Patricia was apparently underestimated even utilizing an operational HWRF configuration with a 2-km grid resolution and assimilating high resolution and high-fidelity near-eyewall observations with a hybrid ensemble variational DA system (Lu et al. 2017b). This result is very likely due to the extraordinarily small size of Patricia, which requests higher model resolution to be used during DA. Meanwhile, during Patricia's lifetime, there are abundant observations in the inner core and outflow regions, including satellite and radar winds, flight level and dropsonde observations, and others. These observations facilitate the assimilation and the verification of analysis and prediction in this study. It is noted that the latest operational HWRF analysis and prediction systems have increased horizontal and vertical resolution relative to the 2015 version. However, no published studies reveal in depth the impact of resolution increase in DA on the TC analysis and forecast.

The manuscript is structured as follows. The second section introduces the type and preprocessing of observations used for assimilation and verification, the model configuration,

and the DA system. In section 3, the experimental design is presented. Section 4 describes and diagnoses the impacts of increased model resolution on TC analysis and prediction and clarifies the relevant mechanisms. Our conclusions are drawn in the final section.

## 2. Observation, data assimilation, and prediction systems

### a. Cases and observations

Patricia occurred over the eastern North Pacific in 2015 with a short lifetime of just 4.5 days. The tropical depression was initially formed at 0600 UTC 20 October 2015, followed by a steady, slow development over 2 days. Around 0000 UTC 22 October, Patricia began to intensify explosively, evolving from a tropical storm (TS) to a category-5 hurricane within a short period of 1.5 days. For details about Hurricane Patricia, the reader is referred to Rogers et al. (2017). Both its RI rate and the strongest maximum surface wind (MSW) valid at 1200 UTC 23 October broke TC's historical records (Knapp et al. 2010; Rogers et al. 2017).

During the life span of Hurricane Patricia, various types of observations were collected. In particular, owing to the Tropical Cyclone Intensity (TCI) field campaign organized by the Office of Naval Research in the 2015 hurricane season, the new High-Definition Sounding System onboard the National Aeronautics and Space Administration aircraft WB-57 released the expendable digital dropsondes (Black et al. 2017) for Patricia (Doyle et al. 2017). The flight altitude is high ( $\sim 18$  km) above the TC to sample the whole depth of both the inner core and outflow regions with unprecedentedly high spatiotemporal resolution (Bell et al. 2016; Doyle et al. 2017). Technical details of the TCI dropsondes can be found in Black et al. (2017). In addition to the TCI dropsondes, a variety of other observations were also collected to depict the spatiotemporal evolution of Patricia. For example, satellite atmospheric motion vector (AMV; Poteat 1973; Franklin et al. 1990; Sears and Velden 2012) observations, flight-level, Stepped Frequency Microwave Radiometer (SFMR), and TDR observations onboard the National Oceanic and Atmospheric Administration WP-3D aircraft (Rogers et al. 2006) were all collected. These observation types are summarized in Table 1, and their temporal distribution during Patricia can be found in Fig. 1a of Lu and Wang (2020).

This paper studied two typical cases during Patricia that initially present as a TS (1800 UTC 21 October; hereafter the “initial-TS case”) and a hurricane (1800 UTC 22 October; hereafter the “initial-hurricane case”), respectively. The two cases allow a comparison of the impacts of model resolution used during DA in distinct scenarios. Meanwhile, the TCI field campaigns were implemented for the two analysis cycles, collecting the high-definition dropsonde observations of zonal ( $U$ ), meridional ( $V$ ) wind, temperature ( $T$ ), and specific humidity ( $Q$ ). Note that in the two cases, only the TCI dropsonde observations are assimilated into the analysis (see “Case study” row of Table 1). One reason is that previous studies (Lu and Wang 2020; Feng and Wang 2019) have demonstrated the assimilation of these TCI dropsonde observations for Patricia dominated the analysis near the vortex due to their high fidelity and relatively complete coverage of TC inner core and outflow

TABLE 1. Descriptions of the configuration of case study (“Case study”) and continuously cycled (“Archived data”) experiments. Columns 3, 6, 7, and 8 are adapted from [Lu and Wang \(2019\)](#).

|               | Model resolution  | Innermost and intermediate domains  | Outermost domain                             | Vortex relocation | Basic model physics   | Observations assimilated                               | Model physics change   |
|---------------|---|---|--|-------------------|---|--|--|
| Case study    | 18, 6, and 2 km and 61 levels; 9, 3, and 1 km and 74 levels | Gridpoint Statistical Interpolation (GSI)-based, continuously cycled, dual-resolution hybrid ensemble-variational (En-Var) data assimilation system for Hurricane Weather Research and Forecasting (HWRF) Model | Global Forecast System (GFS) global analysis | Yes               | Ferrier–Aligo micro-physics scheme; simplified Arakawa–Schubert (SAS) cumulus scheme; HWRF modified surface layer scheme; Noah land surface model; HWRF planetary boundary layer (PBL) scheme; RRTM <sub>G</sub> longwave and shortwave radiation schemes   | High-Definition Sounding System (HDSS) dropsondes only | Reduced “Coac” (horizontal diffusion weight) from 0.75, 3.0, and 4.0 to 0.75, 1.0, and 1.2; further modified turbulent mixing parameterization (vertical diffusivity profile modification) |
| Archived data | 18, 6, and 2 km and 61 levels                               |   |  | No                | TDR, flight level observations, SFMR, CIMSS AMV, HDSS dropsondes, and operational observations (radiosondes, dropwindsondes; aircraft reports; surface ship and buoy observations; surface observations over land; Pibal winds; wind profilers; radar derived velocity–azimuth display wind; WindSat scatterometer winds; integrated precipitable water derived from the global positioning system; satellite radiances from HIRS, AIRS, JASI, GOES, AMSU-A, MHS, and ATMS) |  |  |

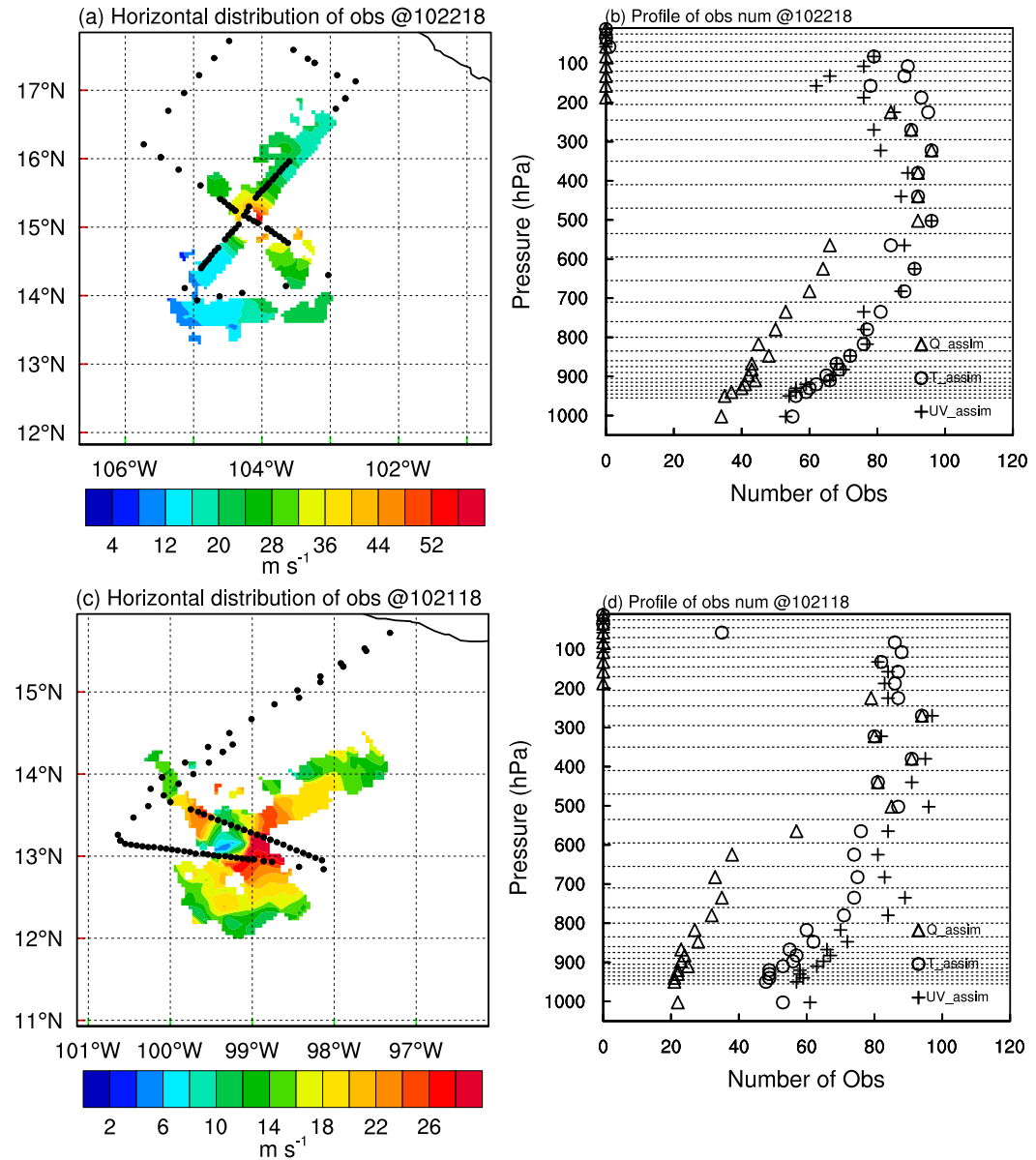


FIG. 1. (a) The three-dimensional spatial distribution of the superrobbed and assimilated TCI dropsonde observations (black dots) overlaid on the Hurricane Research Division (HRD) radar wind speed (shaded; unit:  $\text{m s}^{-1}$ ) at surface, and (b) profile of the number of corresponding TCI dropsonde observations at the initial time (1800 UTC 22 Oct) of the initial-hurricane case. The black dashed lines in (b) are the vertical layers for the superrobbed TCI dropsonde observations. (c),(d) As in (a) and (b), but at the initial time (1800 UTC 21 Oct) of the initial-TS case.

regions throughout the whole TC depth. The other reason is such design enables other available observations (e.g., the flight level, SFMR, and AMV observations) to be used as independent references for the verification of analyses and predictions.

Owing to the high temporal frequency of dropsonde launches ( $\sim 2.5$  min) and their inherent rapid sampling ( $\sim 0.5$  s), there are a huge number of TCI dropsonde observations at a very high horizontal ( $\sim 4$  km; Rogers et al. 2017) and vertical ( $\sim 0.2$  hPa) resolution. Hence, these observations were pre-processed using the superrobbing approach (Alpert and Kumar

2007). Specifically, observations within a defined spatial grid box  $\Delta x \times \Delta y \times \Delta z$  and a defined time interval  $\Delta t$  are averaged to construct a single observation.  $\Delta x$  and  $\Delta y$  are  $0.04^\circ$  ( $\sim 4$  km),  $\Delta z$  nearly spans two model layers, and  $\Delta t$  is 15 min. The selection of these parameters achieves nearly optimal performance in the analysis and prediction of TC intensity (Feng and Wang 2019). The three-dimensional (3D) spatial distribution of the superrobbed and assimilated dropsonde observations is shown in Fig. 1. As mentioned above, the deployed dropsondes almost traverse the TC center at a very high density and extend to the

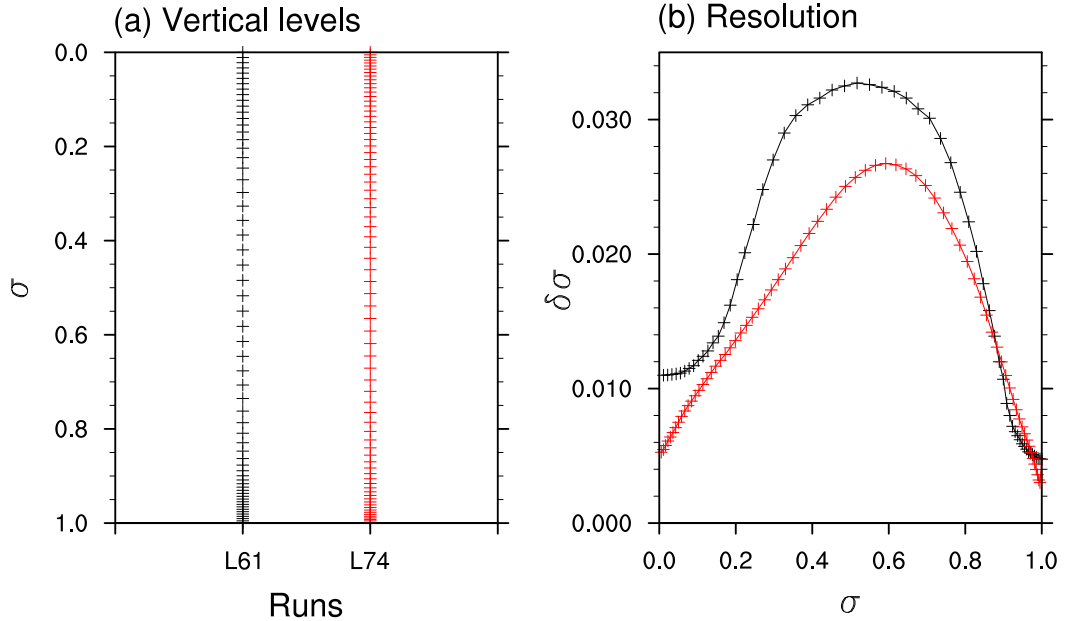


FIG. 2. (a) Distribution and (b) resolution of 61 (black) and 74 (red) vertical model levels.

outflow region (Figs. 1a,c). The observations also cover all vertical levels (Figs. 1b,d), from the sea surface to 100 hPa ( $\sim 16$  km). It is noteworthy that there are much fewer moisture observations (triangle) that passed the quality control in the DA system below 500 hPa and above 200 hPa, possibly due to their low observational quality. For more detailed information about the TCI dropsonde data processing and quality control, see Feng and Wang (2019).

#### b. Model configuration

The HWRF model in the baseline experiments uses the same model resolution as the 2015 operational version (Zhang et al. 2016), which is triply nested with the 18-, 6-, and 2-km ( $0.135^\circ$ ,  $0.045^\circ$ , and  $0.015^\circ$ , respectively) horizontal resolution and contains 61 vertical levels with a 2-hPa model top. The fixed outermost and the two vortex-following moving intermediate and innermost domains within the Arakawa E-grid framework (Tallapragada et al. 2016) are, respectively, configured with  $288 \times 576$ ,  $304 \times 604$ , and  $265 \times 472$  horizontal grid points (approximately  $77^\circ \times 77^\circ$ ,  $27^\circ \times 27^\circ$ , and  $7^\circ \times 7^\circ$ ). The increased horizontal resolution has a narrower grid spacing of about 9, 3, and 1 km ( $0.09^\circ$ ,  $0.03^\circ$ , and  $0.01^\circ$ , respectively) with a reduced domain size ( $50^\circ \times 50^\circ$ ,  $18^\circ \times 18^\circ$ , and  $6^\circ \times 6^\circ$ ). It is slightly higher than the latest updated  $0.099^\circ$ ,  $0.033^\circ$ , and  $0.011^\circ$  in the 2018 operational HWRF (Biswas et al. 2018; Mehra et al. 2018). The enhanced model vertical resolution has 74 levels that follow the same distribution as the 2018 operational HWRF configuration (Biswas et al. 2018; Mehra et al. 2018), except the surface layer thickness ( $\delta\sigma = 0.004747$ ) and the top level (2 hPa) remain the same as those for 61 levels. The comparison of the distribution of 61 (black) and 74 (red) vertical levels is shown in Fig. 2a. The latter (red) increases the model levels at almost all altitudes (near the sea surface and above nearly 900 hPa) relative to the former but keeps the

approximate near-parabolic shape of  $\delta\sigma$  distribution (Fig. 2b). Our preliminary tests show that further increasing the vertical resolution in free forecasts from 74 to 91 levels presents very little impact on the TC intensity forecast for the initial-hurricane case (not shown).

All the experiments used the same HWRF model physics, which is mostly in accordance with those in the 2015 operational HWRF (Tallapragada et al. 2016; see “Basic model physics” column of Table 1). The difference is that, as suggested by Lu and Wang (2019), the modified turbulent mixing parameterization (Zhu et al. 2019) is used in the planetary boundary layer scheme to strengthen the vertical diffusion near the top of the boundary layer. The horizontal diffusion weight (i.e., “Coac”) is also accordingly reduced from 0.75, 3.0, and 4.0 to 0.75, 1.0, and 1.2 (see “Model physics change” column of Table 1) following Lu and Wang (2019). Note that the simplified Arakawa–Schubert cumulus scheme (Han and Pan 2006) is implemented for the outer two domains (i.e., 18- and 6-km grids or 9- and 3-km grids), but not for the innermost domain with the 2 or 1 km grid spacing in both DA cycles and free forecasts as fine-resolution model itself can resolve the convective eddies. It is consistent with the 2015 operational configuration (Tallapragada et al. 2016).

#### c. Data assimilation system

This study used the same DA system as Feng and Wang (2019), which adopts the Gridpoint Statistical Interpolation-based hybrid ensemble Kalman filter (EnKF) variational (EnVar) DA scheme (Wang 2010) for HWRF with continuous cycling and dual-resolution configurations (Lu et al. 2017a,b). Given the 18-, 6-, and 2-km HWRF model configuration as an example, the continuously cycled DA is conducted only for the inner two domains on the 6- and 2-km grids, while the outermost domain (i.e., 18-km grid) directly uses interpolated initial

TABLE 2. Descriptions of designed experiments. “Group 1” increases the model horizontal resolution of first guess (“FG”) or background ensemble (“BE”) or free forecasts from low (“Lh”; 18/6/2 km) to high (“Hh”; 9/3/1 km) given 61 vertical levels. “Fcst” in the parentheses indicates that the forecasts are 6-h higher-resolution (9/3/1 km) model integrations from the analysis in the previous cycle. “Intl” indicates the fields are directly interpolated to the 9/3/1-km resolution from those at 18/6/2-km resolution in BASE at the same valid time. “Group 2” is similar to “Group 1” but enhances the vertical resolution from low (“Lv”; 61 levels) to high (“Hv”; 74 levels) given the 18/6/2-km horizontal resolution.

|         |  | Expt         | FG           | BE         | Analysis     | Free forecast |
|---------|--|--------------|--------------|------------|--------------|---------------|
| Group 1 | Horizontal: 18/6/2 km Vertical: L61<br>Vertical: L61 | BASE         | 18/6/2, L61  | 18/6, L61  | 18/6/2, L61  | 18/6/2, L61   |
|         |  | FG(Hh)BE(Lh) | 9/3/1 (Fcst) | 9/3 (Intl) | 9/3/1        | 9/3/1         |
|         |  | FG(Lh)BE(Hh) | 9/3/1 (Intl) | 9/3 (Fcst) | 9/3/1        | 9/3/1         |
|         |  | FG(Hh)BE(Hh) | 9/3/1 (Fcst) | 9/3 (Fcst) | 9/3/1        | 9/3/1         |
|         |  | BASE(Hh)     | 18/6/2       | 18/6       | 9/3/1 (Intl) | 9/3/1         |
| Group 2 | Horizontal: 18/6/2 km                                |              |              |            |              |               |
|         |  | FG(Hv)BE(Lv) | L74 (Fcst)   | L74 (Intl) | L74          | L74           |
|         |  | FG(Lv)BE(Hv) | L74 (Intl)   | L74 (Fcst) | L74          | L74           |
|         |  | FG(Hv)BE(Hv) | L74 (Fcst)   | L74 (Fcst) | L74          | L74           |
|         |  | BASE(Hv)     | L61          | L61        | L74 (Intl)   | L74           |

conditions from the Global Forecast System analysis at the National Centers for Environmental Prediction (Wang et al. 2013). FGs of the cycled DA at the 6- and 2-km gridded domains use the 3-hourly control forecasts valid at 3-, 6-, and 9-h lead times initialized from the previous DA cycle. The corresponding background error covariance is estimated by 40 6-hourly BE forecasts initialized from the EnKF analyses in the previous DA cycle. To reduce computational expense, the BE is only produced at the 6-km domain but used for the covariance estimation at both the 6- and 2-km gridded domains, adopting the dual-resolution EnVar capability (Lu et al. 2017b). More details about the dual-resolution EnVar DA scheme for HWRF can be found in Lu et al. (2017a,b).

Note that in all experiments the vortices in both FG and BE forecast fields were consistently recentered to the position in the “TCvitals”<sup>1</sup> file using the Vortex Relocation package in HWRF (Tallapragada et al. 2016). This is a routine procedure applied in most studies of TC assimilation for HWRF (e.g., Pu et al. 2016; Lu et al. 2017b). The Vortex Intensity modification package in HWRF is not used since a large amount of inner core observations are assimilated (Pu et al. 2016; Lu and Wang 2019). For the intermediate and innermost domains, the full ensemble covariance was used without combining the static covariance since the default static covariance, characterized by the multivariate large-scale spatial coherence, showed no improvement to the assimilation of the finescale inner structure of TCs (Schwartz 2016; Lu et al. 2017b). The aforementioned information on the observing, DA, and prediction systems used for the experiments was summarized in Table 1.

### 3. Experimental design

To address the impact of increasing the model horizontal or vertical resolution of FG or BE on TC analysis and prediction, a

series of experiments were carried out based on the analysis and prediction systems for HWRF. The model data used in these case-study experiments were drawn from the archived data of continuously cycled DA for Patricia run by Lu and Wang (2019; details can be found in “Archived data” row in Table 1). It ranges from 1800 UTC 20 October to 1200 UTC 24 October with a 6-h DA cycle using the operational HWRF model configuration (i.e., 18-, 6-, and 2-km horizontal resolutions and 61 vertical levels) and the DA system introduced in section 2c. All available observations were assimilated at each analysis time, including operational observations and others from unconventional instruments (e.g., TDR, flight-level, SFMR, TCI dropsonde, and AMV observations) if available (see third row in “Observations assimilated” column).

In this study, the FG and BE forecasts in the baseline experiment (BASE) for the two cases are short-range model forecasts at the 18-, 6-, and 2-km resolution using the model configuration in section 2b initialized from the archived control and EnKF analysis data, respectively, in the previous cycle, i.e., at 1200 UTC 21 October for the initial-TS case and 1200 UTC 22 October for the initial-hurricane case (see Table 2). Only the TCI dropsonde observations are assimilated in the two cases.

Two groups of experiments were designed to investigate the individual impact of increasing horizontal resolution from 18, 6, and 2 km to 9, 3, and 1 km (Group 1) and vertical resolution from 61 to 74 levels (Group 2). In each group, the impact of the increased resolution for FG and BE are separately examined. Specifically, in Group 1, FG(Hh)BE(Lh) investigates the impact of FG with increased horizontal resolution relative to BASE. Its FG is generated by integrating the 9-, 3-, and 1-km gridded initial condition in the previous cycle (i.e., 1200 UTC 21 and 22 October), which is interpolated from the corresponding archived analysis state at the 18-, 6-, and 2-km grid spacing. This design ensures that the FG fields of BASE and FG(Hh)BE(Lh) are initialized from the same analysis although they use different resolution during the FG model integration. FG(Hh)BE(Lh) has the same BE as BASE. In contrast, FG(Lh)BE(Hh) is designed to investigate the impact of BE with increased horizontal resolution. Therefore, its BE

<sup>1</sup> A tcvitals file is a small data file provided by the National Hurricane Center (NHC) that contains the current operational estimate of the storm’s center location, intensity, and central pressure (Liu et al. 2006; Gopalakrishnan et al. 2010).

is a set of model integrations with increased horizontal resolution (i.e., 9 and 3 km) initialized from the interpolated archived ensemble analyses in the last cycle (i.e., 1200 UTC 21 and 22 October), while FG is the same as that in BASE. As to FG(Hh)BE(Hh), both FG and BE are from the integrations with increased resolution to reveal their combined effects. The initial analysis of BASE(Hh) is the same as that of BASE but is interpolated to the 9-, 3-, and 1-km grid spacing for a high-resolution free forecast. Group 2 is similar to Group 1 but is focused on the increased vertical resolution without changing the horizontal resolution relative to BASE. More details of the experiments can be found in Table 2.

## 4. Results

### a. Impact of increased model resolution on TC analyses

#### 1) TC INTENSITY AND STRUCTURE IN ANALYSES

The initial TC intensity in terms of the MSW in all experiments was summarized and compared to the best track estimation<sup>2</sup> (black cross) in Fig. 3. Their uncertainties are represented by adding and subtracting the respective spread of MSW among 40 EnKF analysis members at the intermediate domain. The TC intensity difference between two experiments is considered statistically significant if it exceeds their uncertainties. Figure 3 shows that the MSW in the BASE analyses (red triangle) is significantly underestimated, about 9 and 6 m s<sup>-1</sup> weaker than the reference in the initial-hurricane and initial-TS cases, respectively. Nonetheless, increasing the horizontal or vertical resolution of FG or BE can generally improve the analyzed intensity of Patricia. The two exceptions are increasing the FG horizontal (i.e., FG(Hh)BE(Lh), orange solid circle) or vertical (i.e., FG(Hv)BE(Lv), orange hollow circle) resolution in the initial-TS case (Fig. 3b), with less than 1 m s<sup>-1</sup> differences from BASE. This result suggests the limited impact of increasing model resolution on the FG field for a weak TC (see Figs. 7g–i).

Interestingly, increasing the FG resolution produces a stronger TC initial intensity than increasing the BE resolution in the initial-hurricane case for either horizontal or vertical resolution, whereas the opposite is true for the initial-TS case (cf. orange and green solid or hollow circles in Fig. 3). Such difference is mainly because increasing the FG resolution shows a larger effect in improving the representation of TC structure and intensity for the hurricane stage than the TS stage [see more discussion in section 4a(3)]. In the initial-hurricane case, enhancing horizontal resolution produces a stronger TC initial intensity than vertical resolution for FG or BE (cf. solid and hollow circles with the same color in Fig. 3a). However, the differences between the impact of increasing horizontal and vertical resolution are mixed in the initial-TS case. This result suggests increasing horizontal resolution may have a stronger effect on TC analyses than increasing vertical resolution for

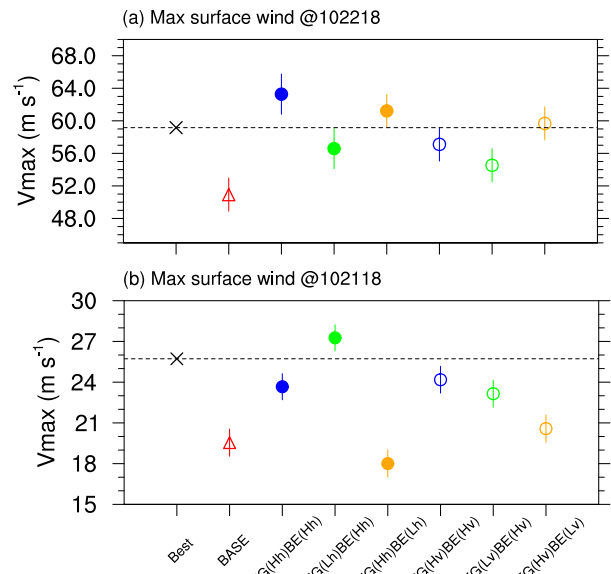


FIG. 3. The initial TC maximum surface wind (MSW) of all the experiments in the (a) initial-hurricane and (b) initial-TS cases with the best track estimation (black cross) as a reference. The uncertainty is presented by adding and subtracting the ensemble spread of MSW in the ensemble analysis.

intense TCs. FG(Hh)BE(Hh) (blue solid circle) exhibits the strongest analyzed intensity in the initial-hurricane case but overshoots compared to the best track (cross).

The surface (10 m) wind speeds in analyses are further verified against the SFMR observations (Fig. 4). In the initial-hurricane case, most experiments present stronger and more accurate initial surface wind speed along the transect than BASE (red solid line), including all the six on the northeastern branch and four out of six on the southwestern branch. As in Fig. 3a, increasing the horizontal resolution of either FG or BE produces stronger eyewall wind than increasing the vertical resolution in the initial-hurricane case (cf. solid and dashed lines with the same color in Fig. 4a). FG(Hh)BE(Hh) (blue solid line) overall displays the most accurate surface wind speed in the eyewall along the transect. Despite the improved analyzed eyewall wind by increasing model resolution, their eyewall sizes only present slight improvement in the initial-hurricane case. The oversized analyzed eyewalls suggest that assimilating high-resolution near-eyewall observations may still not be enough to fully correct the eyewall size if it is incorrectly simulated in FG (see Figs. 7a–c). In the initial-TS case with a much weaker TC (Fig. 4b), the experiments FG(Hh)BE(Hh), FG(Lh)BE(Hh), FG(Hv)BE(Hv), and FG(Lv)BE(Hv) have stronger (up to 6 m s<sup>-1</sup>) surface wind speed than BASE near the 40-km radius on the northeastern side as in Fig. 3b. On the southwestern side, FG(Hv)BE(Hv) (blue dashed line) performs the best followed by FG(Hv)BE(Lv) (orange dashed line), whereas others are similar to BASE. The comparison between the two cases in Figs. 3 and 4 indicates that the relative importance between the increased horizontal and vertical resolution and

<sup>2</sup> Best track data is the best estimate of tropical cyclone position and intensity. It is provided by the U.S. NHC (<http://www.nhc.noaa.gov/data/#hurdat>).

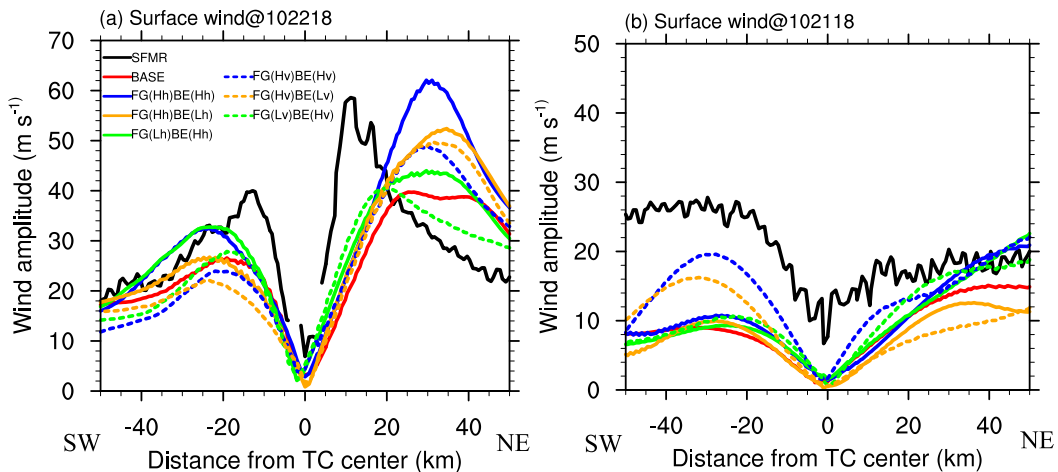


FIG. 4. Surface (10-m) wind speed in the analyses of the (a) initial-hurricane and (b) initial-TS cases verified against the stepped frequency microwave radiometer (SFMR) observations.

between the increased FG and BE resolution varies with the phase of the TC.

The MSW evaluated in Fig. 3, as an indicator of TC intensity, may not be able to evaluate the overall structure of eyewall wind. Therefore, we calculated the vertical profile of azimuthally averaged wind speed at the radius of maximum wind (RMW) from the TC center in the analysis fields (Fig. 5). Figure 5a shows that in the initial-hurricane case, all the experiments with increased model resolution present overall stronger eyewall wind in the analyses than BASE near 1000 hPa. The differences from BASE increase with height, reach the maximum at the level of the strongest wind (~950 hPa) and gradually decrease upward. Note that the relative strength of the azimuthally averaged wind speed at low levels (1000–700 hPa) for all experiments are the same as that of the initial MSW (Fig. 3a) and that of the eyewall wind along

the northeastern transect (Fig. 4a). Some experiments in the initial-TS case (Fig. 5b) also exhibit overall intensified eyewall wind near the surface relative to BASE, including FG(Hv)BE(Hv), FG(Hh)BE(Hh), FG(Lh)BE(Hh), and FG(Lv)BE(Hv). They are also consistent with the MSW results in Fig. 3b. However, unlike the initial-hurricane case, the eyewall wind differences among the experiments become rather nonlinear toward higher levels in the initial-TS case. The large maximum wind speed in upper troposphere in BASE and FG(Hh)BE(Lh) (Fig. 5b) remains to be explored.

AMV data are the only available observations that can be used to verify the kinematic structure at the TC outflow layer. Figure 6 shows the AMVs (arrow) and the radial component relative to the TC center (dots) near 150 hPa (Fig. 6a) at 1800 UTC 22 October and the wind analysis (arrow) at the same level in all experiments (Figs. 6b–h) overlaid on the

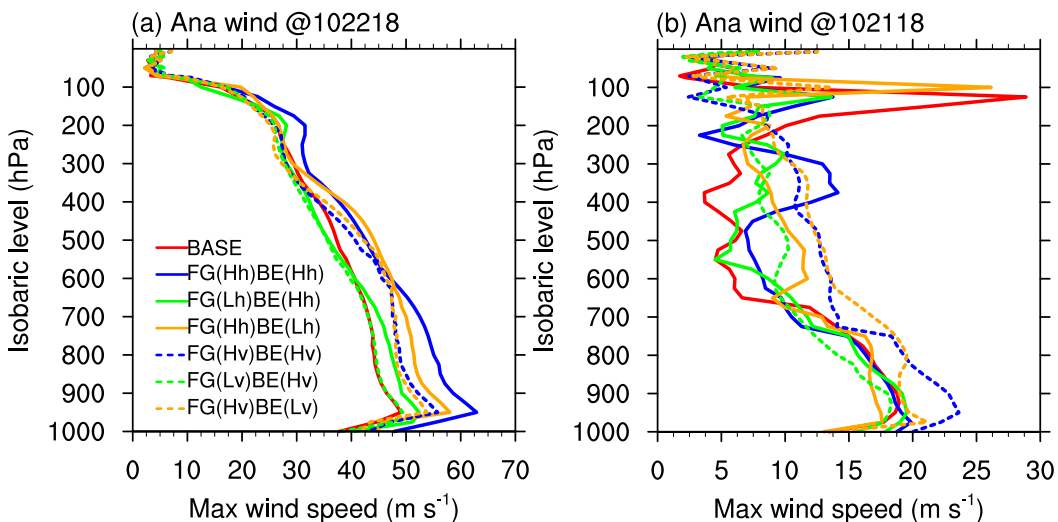


FIG. 5. The vertical profile of azimuthally averaged wind speed at the radius of maximum wind (RMW) in the analysis fields for individual experiments in the (a) initial-hurricane and (b) initial-TS cases.

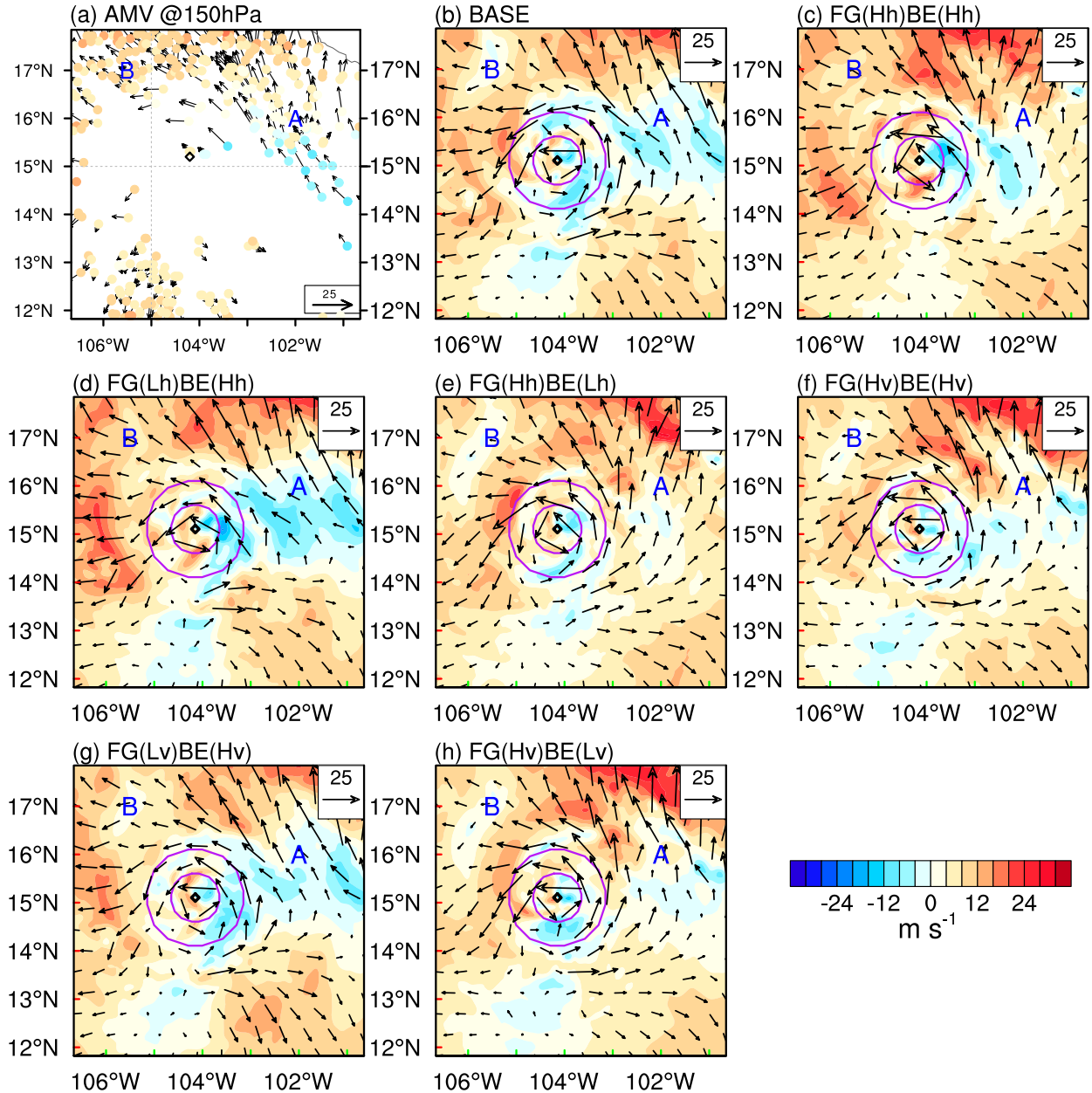


FIG. 6. (a) Atmospheric motion vector (AMV) observations (arrows) and the radial component (dots) near 150 hPa at 1800 UTC 22 Oct, and (b)–(h) the wind vector analysis (arrows) at the same level in all experiments overlaid on the corresponding radial component (shaded) in the initial-hurricane case. Black square marks the TC center. Purple circles denote the 50- and 100-km radii from the center.

corresponding radial component (shaded) in the initial-hurricane case. Almost all the AMVs are outside the 100-km radius from the TC center, providing limited value for the verification of Patricia's inner structure. All the experiments consistently present a well-organized outflow beyond the 100-km radius, preceding the subsequent rapid development of Patricia, but some differences still exist. FG(Hh)BE(Hh) shows an overall stronger outflow than BASE from the near-TC region (50–100 km; purple circles) to the outer environment beyond the 100-km radius (cf. Figs. 6c and 6b),

consistent with Fig. 5a. The stronger outflow is jointly contributed by the increased horizontal resolution of FG (Fig. 6e) and BE (Fig. 6d). The northeastern environmental outflow of FG(Hh)BE(Hh) is too strong compared to that of BASE according to the observations (cf. Figs. 6c and 6b), possibly because it is overamplified in FG with increased horizontal resolution (cf. Figs. 6e and 6c). Nonetheless, increasing the FG horizontal resolution shows some positive impact on the upper-level wind analysis, for example, correcting the negative radial wind near marker "A" in BASE and FG(Lh)BE(Hh) to

positive in FG(Hh)BE(Lh) and FG(Hh)BE(Hh) (cf. Figs. 6b,d and 6c,e).

The stronger outflow to the southwest of TC in FG(Hh)BE(Hh) than BASE is attributed to the increased BE horizontal resolution (cf. Figs. 6c and 6d). Increasing the horizontal resolution of BE also displays some positive impact, for example, the correct positive radial wind near marker “B” in FG(Lh)BE(Hh) and FG(Hh)BE(Hh) relative to the negative in BASE. Interestingly, for the same type of experiments, the wind analyses with increased vertical resolution show similar structure but overall weaker amplitude to those with increased horizontal resolution (cf. Figs. 6c,f, 6d,g, and 6e,h, respectively). This may indicate that increasing model vertical resolution has an analogous but weaker effect on short-range background forecasts than horizontal resolution.

## 2) IMPACT OF INCREASING RESOLUTION OF FIRST GUESS

To understand the impact of the increased FG resolution on the analyzed wind field, we first compared the near-surface (1000-hPa) wind amplitude (shaded) fields in FG using different model resolutions (Fig. 7). Their corresponding analyses using the same BE are also shown. In the initial-hurricane case, both the increased horizontal and vertical model resolutions obviously strengthen and improve the overall TC eyewall wind in FG (cf. Figs. 7b,c and 7a), reaching a nearly  $10 \text{ m s}^{-1}$  increase for the MSW in the eyewall (blue crosses). It leads to more intense analyzed wind amplitudes in the near-surface eyewall of FG(Hh)BE(Lh) and FG(Hv)BE(Lv) (cf. Figs. 7e,f and 7d; see more discussions on Fig. 8), which is consistent with Figs. 3a and 5a. The analyzed structures of the eyewall wind amplitude in FG(Hh)BE(Lh) and FG(Hv)BE(Lv) also become more realistic than in BASE when compared to the Hurricane Research Division (HRD 2015) radar wind analysis (shaded in Fig. 1a). For example, the MSW (blue crosses) of the former two are located in the eastern eyewall consistent with those observed in Fig. 1a, while the latter is located in the northwestern eyewall. In contrast, the TC intensification in FG due to the resolution increase is much less significant in the initial-TS case (cf. Figs. 7h,i and 7g), with up to  $3 \text{ m s}^{-1}$  amplifications for MSW (blue crosses). The wind amplitudes near the eyewall in all the three FG fields are apparently weaker than the observation (Fig. 1b). The analyzed eyewall wind amplitudes of FG(Hh)BE(Lh) and FG(Hv)BE(Lv) thus only show little distinction from that of BASE as in Figs. 3b and 5b.

With the exception of increasing the FG vertical resolution in the initial-TS case (cf. Fig. 7i and 7g), the eyewalls in FGs generally slightly shrink ( $\sim 7 \text{ km}$ ) when the model resolution is increased (cf. Figs. 7b,c,a and 7g,h). The smaller eyewall sizes in FGs may help reduce the eyewall sizes in their analyses. Nonetheless, the eyewall sizes in the analyses are still overestimated for all the experiments in the initial-hurricane case as in Fig. 4a. It may be due to the model physics deficiency that constrains the formation of an extraordinarily small TC like Patricia in FGs.

We further investigated the mechanism of how the increased FG resolution influences TC analysis fields. Given that increasing horizontal resolution in free forecasts produces much

more TC forecast improvement than increasing the vertical resolution (see section 4b), the mechanism of the impact from increased resolution of FG [section 4a(2)] and BE [section 4a(3)] on the DA performance is clarified primarily using horizontal resolution as an example. The analysis is the sum of the FG forecast and the analysis increment (AI; i.e., the difference between the analysis and FG). It can be described by the following relation:

$$x^a = x^f + x', \quad (1)$$

where  $x^a$ ,  $x^f$ , and  $x'$  denote analysis, FG, and AI fields, respectively. For two experiments to be compared, their differences in each term satisfy a similar relation:

$$\Delta x^a = \Delta x^f + \Delta x', \quad (2)$$

where  $\Delta$  signifies the difference. Following Eq. (2), to address the individual contribution of FG and AI to the analysis associated with the increased FG resolution, Fig. 8 shows the differences (shaded) between FG(Hh)BE(Lh) and BASE in the FG, AI, and analysis fields of 1000-hPa  $U$  (Figs. 8a–c) and 300-hPa  $T$  (Figs. 8d–f) in the initial-hurricane case overlaid by the original fields of BASE (contour).  $T$  at 300 hPa is shown as it approximately matches the level of the maximum warm core (see Fig. 15).

The FG(Hh)BE(Lh) analyses show apparently intensified eyewall winds (Fig. 8c) and a warmer inner core (Fig. 8f) than BASE, consistent with the performance of their TC intensity (Fig. 3a). The FG differences of  $U$  wind present similar structure and amplitude to the analysis differences near the eyewall, especially for the eastern and northeastern parts (cf. Figs. 8a and 8c). However, the AI differences show opposite signs for these eyewall regions (cf. Figs. 8b and 8c), especially at the MSW position of FG(Hh)BE(Lh) (green cross). In contrast, the warmer inner core (near the red square) analysis in FG(Hh)BE(Lh) is mainly contributed by the differences of AI (cf. Figs. 8f and 8e). This result indicates that increasing the FG resolution could have a positive impact on the analyses from two aspects. One is to directly improve the depiction of the TC structure and intensity in FG, especially the finescale features near the eyewall. The other is attributed to the reduced error of FGs relative to observations at finer scales, reducing the observational innovation (i.e., observation minus FG) that is a critical term in DA (Wang 2010).

## 3) IMPACT OF INCREASING RESOLUTION OF BACKGROUND ENSEMBLE

This section analyzes how the increase of the BE resolution itself improves the TC initial intensity. Increasing the BE resolution can impact the estimation of background error covariance, and thus influence the AI in two major aspects. One aspect is the estimation of background ensemble variance used to quantify the uncertainty of FGs. Therefore, we compared the ensemble spread (i.e., the square root of background ensemble variance) against the absolute value of observational innovation in BASE, FG(Lh)BE(Hh), and FG(Lv)BE(Hv) with the same FG in both cases (not shown). Verifying against observations is a widely used approach to estimate the FG

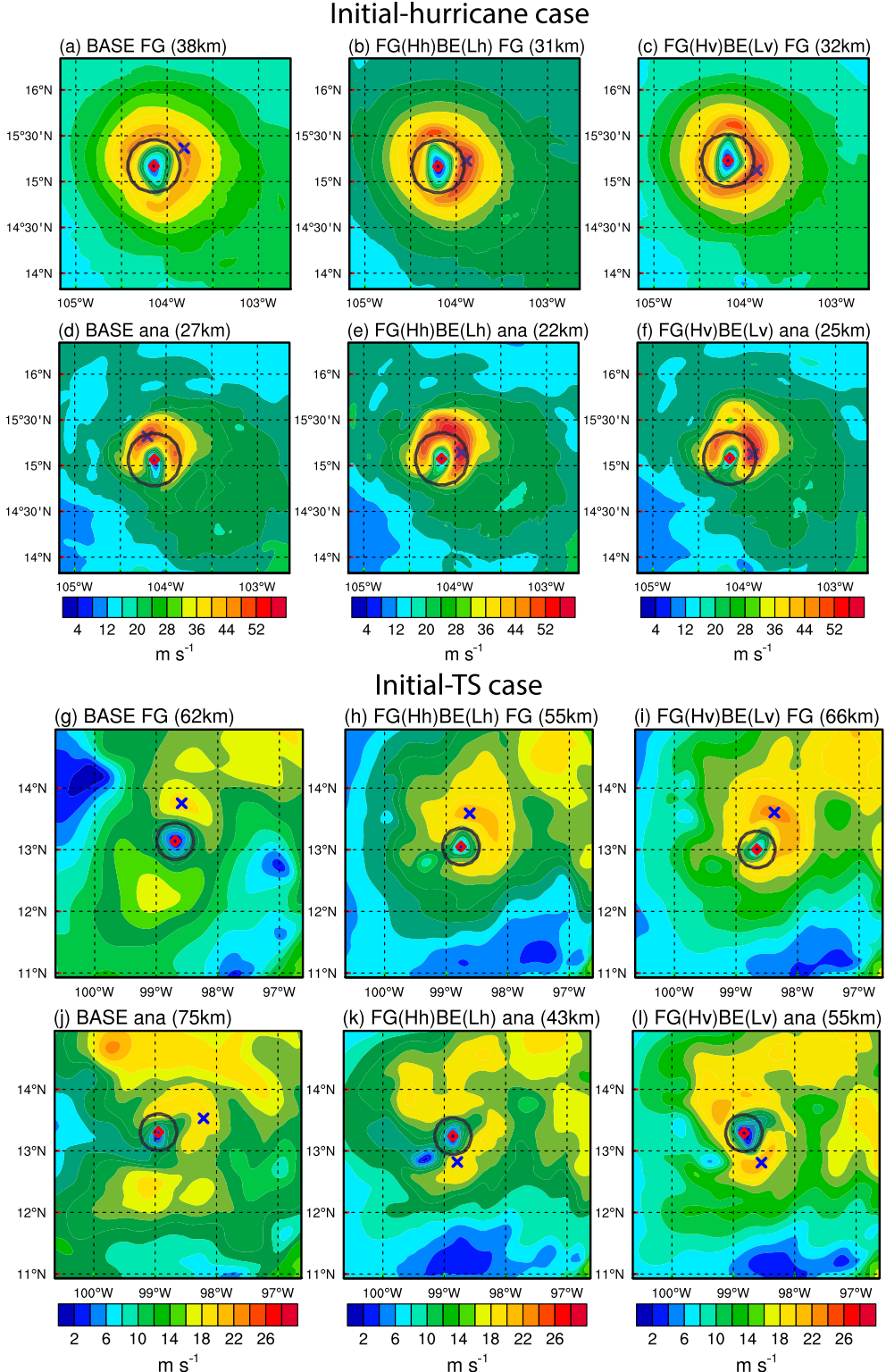


FIG. 7. Wind amplitude (shaded) at 1000 hPa in (a)–(c) the first guess (FG) fields of BASE, FG(Hh) BE(Lh), and FG(Hv)BE(Lv) in the initial-hurricane case as well as (d)–(f) the corresponding analysis fields. (g)–(l) As in (a)–(f), but for the initial-TS case. The blue cross and red square denote the positions of MSW and TC center, respectively. The black circle is the 30-km radius from the center. The numbers in the parenthesis are the TC eyewall sizes.

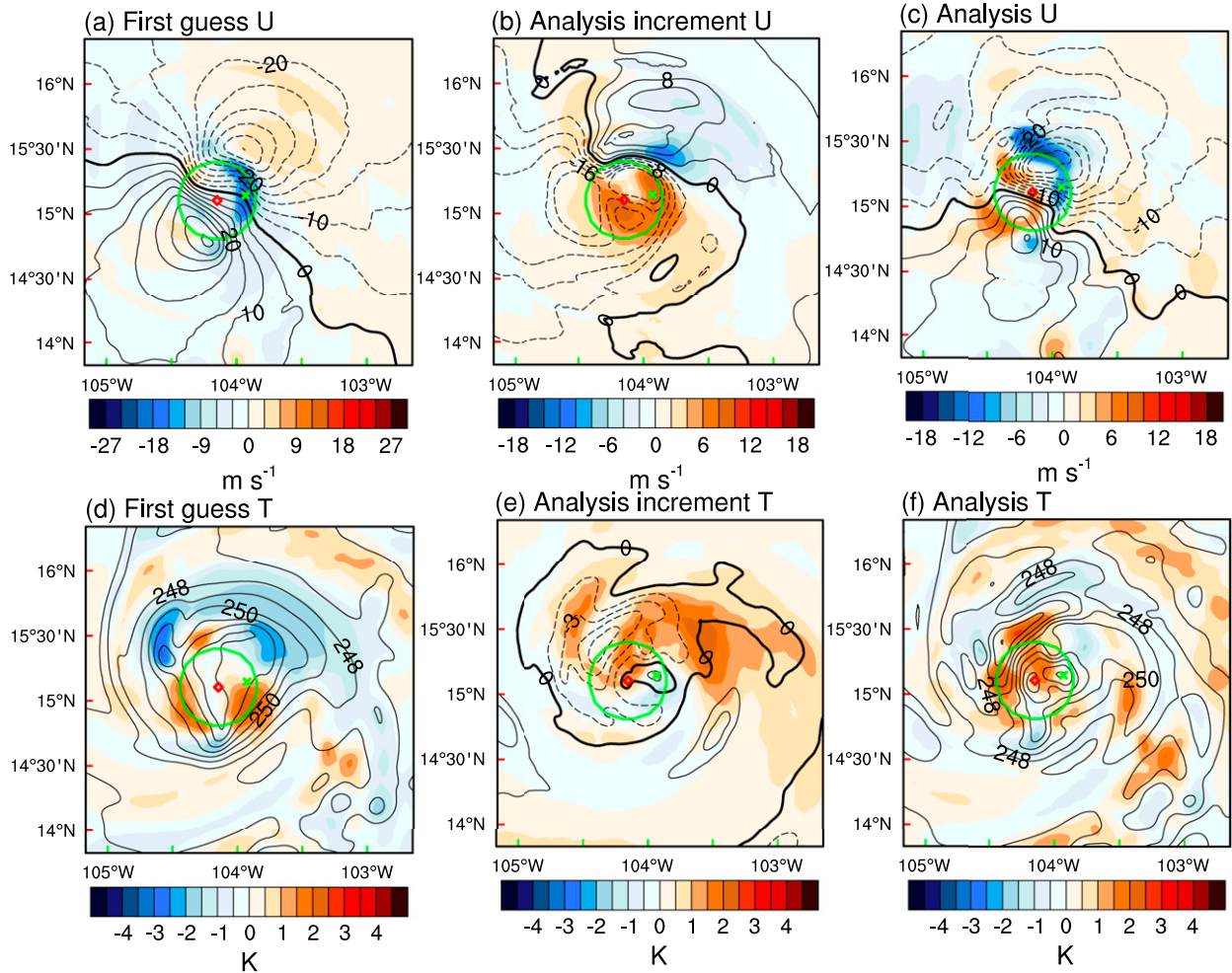


FIG. 8. Differences (shaded) of the (a) first guess, (b) analysis increment, and (c) analysis of 1000-hPa  $U$  wind between the experiments FG(Hh)BE(Lh) and BASE overlaid by the corresponding original field of BASE in the initial-hurricane case. (d)–(f) As in (a)–(c), but for 300-hPa  $T$  in the same case. The green cross and red square denote the positions of MSW and TC center in FG(Hh)BE(Lh), respectively. The green circle is the 30-km radius from the center.

uncertainty (e.g., Wang and Bishop 2003; Houtekamer et al. 2005). The results (not shown) indicate that neither increasing the horizontal resolution nor the vertical resolution of BE can boost the level of the ensemble spread to quantify the FG error for all the variables. Especially near the TC eyewall region, the spread-error correlation is around zero or even negative for all of the experiments. This signifies that it remains rather challenging to estimate the FG error magnitudes near the TC eyewall with sharp kinematic and thermodynamic gradients by using a limited size of BE.

In addition to the estimation of background error variance, the background ensemble covariance offers the 3D spatial and cross-variable correlation between given observations and grid points to quantify the extent and range of observational impact. Here, we use wind variables in the initial-hurricane case as an example to clarify the impact of the background ensemble correlation on AI. Figures 9a and 9d show the differences of the  $U$ - and  $V$ -wind analyses near the surface (1000 hPa; shaded) between FG(Lh)BE(Hh) and BASE overlaid by the corresponding

analysis field of BASE (contour). Other panels in Fig. 9 show the horizontal correlation fields (contour) at the same level and the positive (red triangles) and negative (blue circles) observational innovations below 800 hPa. The horizontal correlation structure is centered at the MSW position of FG(Lh)BE(Hh) (green cross) where the negative differences of  $U$  (Fig. 9a) and  $V$  (Fig. 9d) analyses signify an increase of TC intensity. Such difference is an accumulated impact of the innovation of the observations near the given grid point. The strength and range of the influence of innovations on a given grid are partially determined by the spatial correlation of the background ensemble between the given grid point and the nearby observation locations. Comparing Figs. 9b,c and 9e,f, higher resolution BEs give an overall similar spatial correlation structure (contour) as in BASE but with qualitatively more finescale features (e.g., the thick black contour of 0.4). The more realistic and accurate correlation structure in FG(Lh)BE(Hh) allows more negative (e.g., blue boxes in Figs. 9b and 9c) or less positive

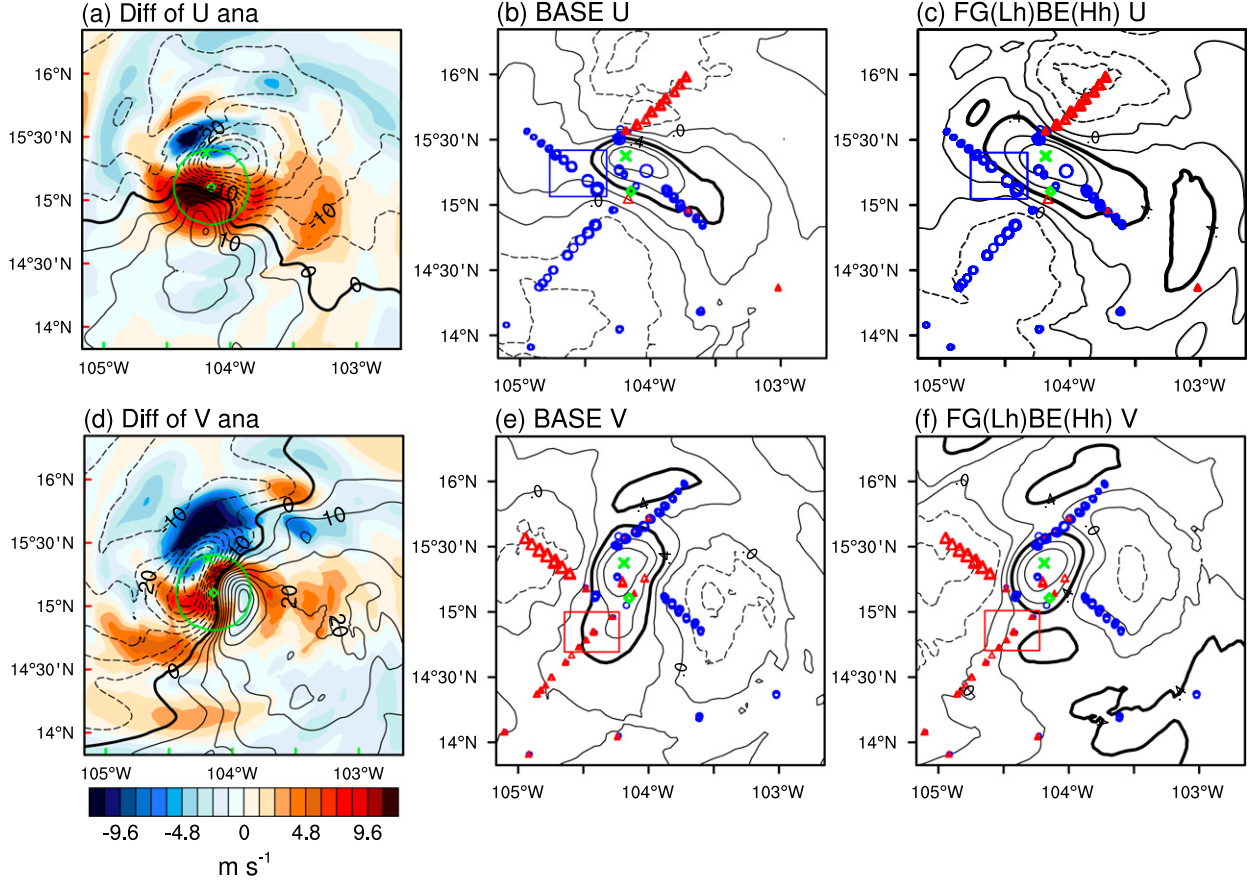


FIG. 9. (a) Difference (shaded) of the analysis of 1000-hPa  $U$  wind between the experiments FG(Lh)BE(Hh) and BASE overlaid by the corresponding original field of BASE in the initial-hurricane case. (b),(c) The horizontal correlation fields (contour) at the same level and the positive (red triangles) and negative (blue circles) observational innovations below 800 hPa for  $U$  wind of BASE and FG(Lh)BE(Hh) in the initial-hurricane case, respectively. (d)–(f) As in (a)–(c), but for  $V$  wind. The correlation field is centered at the MSW position of FG(Lh)BE(Hh) (green crosses). The green square and circle represent the TC center and 30-km radius.

(e.g., red boxes in Figs. 9e and 9f) observational innovations to be ingested into the AI of the wind analysis at the given location (green cross). Such effect thereby contributes to a stronger MSW in FG(Lh)BE(Hh). Overall, the improved TC analyses by increasing the BE resolution is dominated by the more realistic finescale background error correlation estimation rather than the background error variance estimation.

Recall that in Fig. 3 the amplifications of analyzed MSW by increasing the BE resolution are similar between the initial-hurricane and initial-TS cases. In contrast, as shown in Figs. 3 and 7, increasing the FG resolution presents larger impact on TC structure and intensity in FGs and analyses for an intense hurricane case than a tropical storm case. The two points above may explain the result in Fig. 3 that increasing the FG resolution is more effective in improving the analyzed eyewall wind in the initial-hurricane case but increasing the BE resolution is more effective in the initial-TS case.

#### 4) WIND-PRESSURE RELATIONSHIP IN ANALYSES

The use of different model resolutions for FG or BE may influence the physical and dynamical balance in the analyzed

TC vortices. Previous literatures (e.g., Willoughby 1990) have demonstrated that the wind-pressure relationship of TC vortices approximately satisfies the gradient wind balance. In this subsection, we evaluate the impact of increasing resolution during DA on wind-pressure relationship in the analyzed vortices for an initial-hurricane case. The metric used is the net radial force field  $F$  as defined by Smith et al. (2009), Pu et al. (2016), and Lu and Wang (2019). A closer-to-zero value of  $F$  indicates a better approximation to the gradient wind balance.

Figure 10 shows the net radial force field  $F$  of the analyzed TC vortices for BASE (Fig. 10a), FG(Hh)BE(Hh) (Fig. 10b), FG(Lh)BE(Hh) (Fig. 10c), and FG(Hh)BE(Lh) (Fig. 10d) in the initial-hurricane case. Figure 10 shows that the four experiments similarly manifest an overall supergradient ( $F > 0$ ) wind-pressure relationship near the eyewall (blue lines), with the maximum at the inner edge of eyewalls. FG(Lh)BE(Hh) (Fig. 10c) has closer horizontal resolution for BE and FG (3 vs 2 km) compared to BASE (6 vs 2 km), and thus exhibits smaller  $F$  values, i.e., a better gradient wind balance. In contrast, FG(Hh)BE(Hh) and FG(Hh)BE(Lh) (Figs. 10b,d) display similarly larger deviation from the gradient wind balance than

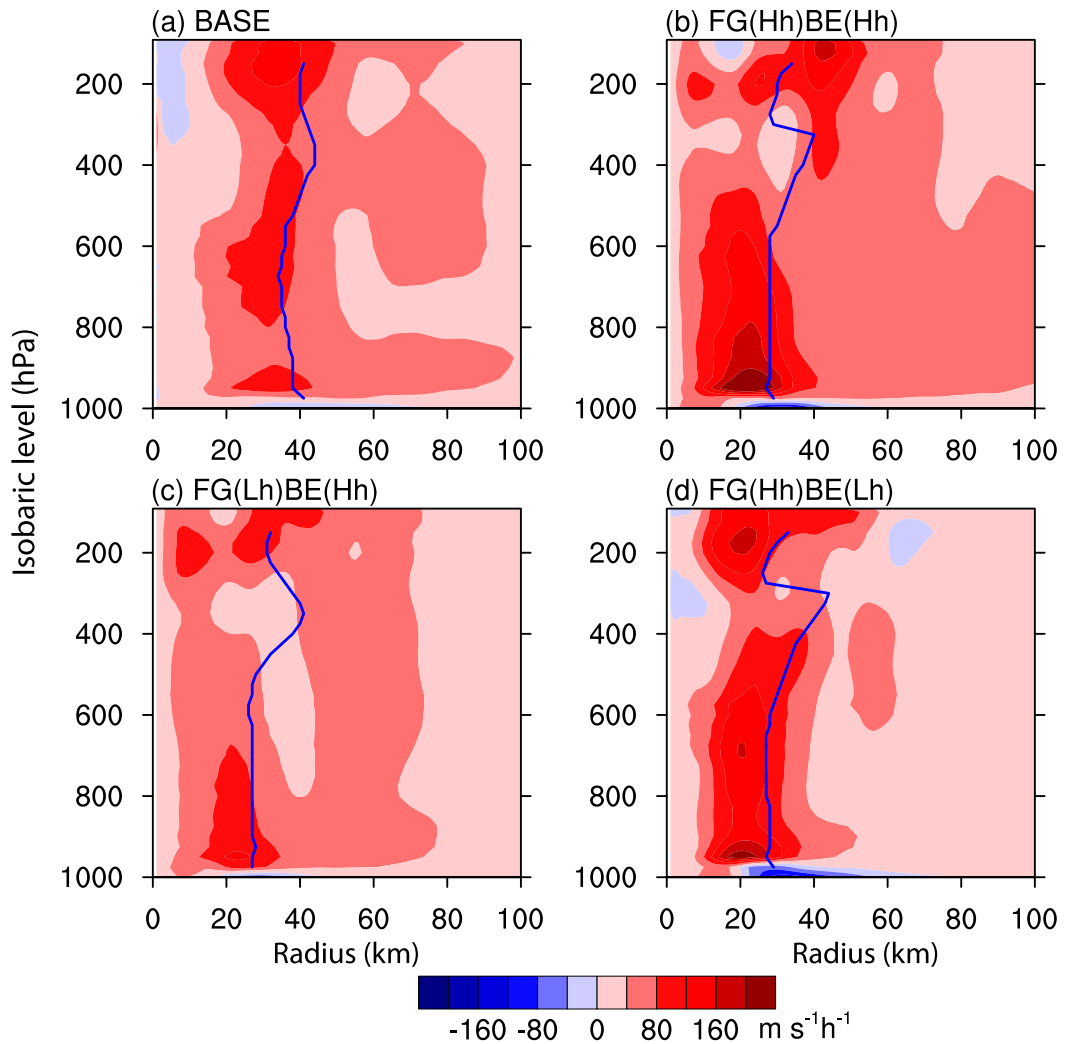


FIG. 10. The azimuthally averaged net radial force (unit:  $\text{m s}^{-1} \text{h}^{-1}$ ) of TC analyses experiments (a) BASE, (b) FG(Hh)BE(Hh), (c) FG(Lh)BE(Hh), and (d) FG(Hh)BE(Lh).

BASE and FG(Lh)BE(Hh). Such larger deviation may be associated with the increased finer-scale features resolved in higher-resolution FG (from 2 to 1 km). Despite the supergradient wind–pressure relationship, none of the experiments appear to experience “spindown” problem that often influences TC intensity forecasts in previous studies (e.g., Pu et al. 2016; Lu and Wang 2019).

#### *b. Impact of increased model resolution on TC intensity prediction*

The results in section 4a(1) demonstrate that the analyzed TC intensity and structure can be improved by increasing the model resolution of FG or BE. This section compares the intensity forecasts initialized from these analyses (Fig. 11) to determine whether such initial improvement can help the subsequent intensity forecasts. For ease of comparison, Table 3 summarizes the error magnitude of the TC initial and peak MSW (i.e., the strongest TC MSW during the forecast) in all experiments normalized by the corresponding error magnitude

of BASE in individual cases. Herein, except for the BASE experiment on the resolution of 18, 6, and 2 km and 61 vertical levels, the free forecasts in all other experiments are run on the increased horizontal (9, 3, and 1 km) or vertical (74 levels) resolution. BASE(Hh) and BASE(Hv) are first briefly examined against BASE to evaluate the impact of free forecast model resolution. The comparisons of BASE(Hh) and BASE(Hv) against other experiments (except BASE) are intended for isolating the impact of model resolution used during DA. BASE(Hh) presents a faster TC intensification rate and a more accurate and stronger peak intensity than BASE (cf. purple and red solid lines) in both cases (Figs. 11a,c), while BASE(Hv) (purple dashed line) shows no improvement or even worse performance (Figs. 11b,d). Interestingly, the intensity forecasts with increased horizontal resolution in free forecasts all reach a peak intensity that is much stronger than those with higher vertical resolution in the same case (cf. Figs. 11a,b and 11c,d) except FG(Hh)BE(Hh) (blue solid line) in the initial-TS case. This indicates that increasing model

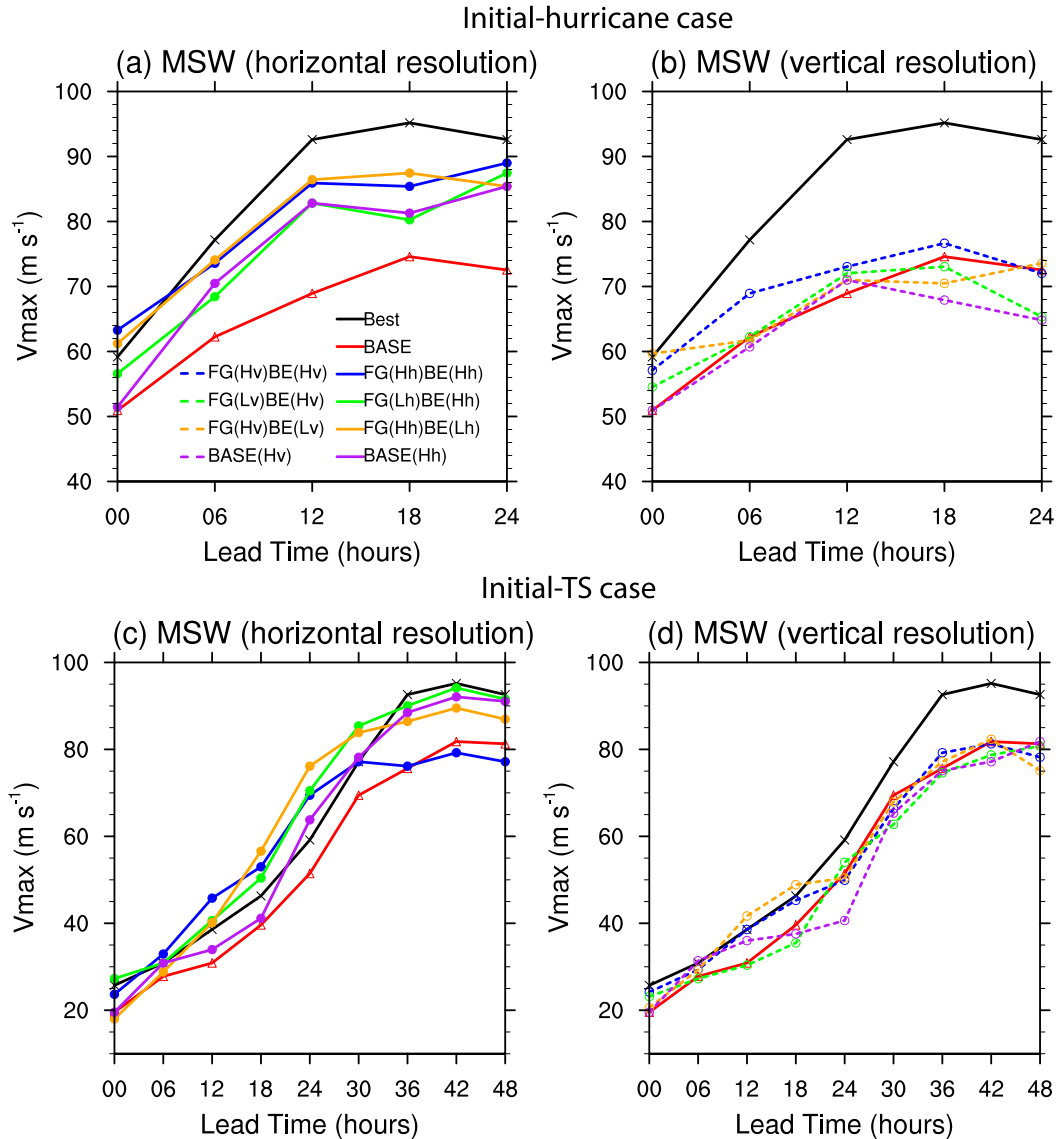


FIG. 11. MSW forecasts as a function of lead time for the experiments in the (a),(b) initial-hurricane and (c),(d) initial-TS cases. Black solid line represents the best track estimation.

horizontal resolution may be systematically more effective than increasing vertical resolution for improving the intensity forecasts of strong TCs like Patricia.

In the initial-hurricane case (Fig. 11a), the experiments FG(Hh)BE(Hh) and FG(Hh)BE(Lh) (blue and orange solid lines) provide similar TC intensity forecasts within the first 18 h, reaching a more intense and accurate TC peak intensity than BASE(Hh) (purple solid line). It is probably associated with their improved analyzed TC intensity (see Table 3). FG(Lh)BE(Hh) (green solid line) has similar accuracy of TC initial MSW as FG(Hh)BE(Lh) (0.31 vs 0.25 in Table 3) but presents no improvement relative to BASE(Hh) in the subsequent forecasts (cf. green and purple solid lines in Fig. 11a). It implies that the effects of increasing the FG horizontal resolution may primarily explain the superior performance of

FG(Hh)BE(Hh) in the initial-hurricane case. In the initial-TS case (Fig. 11c), the impact from the more accurate initial conditions can extend to 24 h [cf. FG(Hh)BE(Hh) (blue solid line) and FG(Lh)BE(Hh) (green solid line) versus BASE(Hh) (purple solid line)], although the TC intensity is overestimated relative to the best track. In particular, FG(Lh)BE(Hh) (green solid line) reaches the most accurate peak intensity forecast, probably associated with its most accurate initial TC intensity (see Table 3). This result suggests the possibly more important role of increasing the horizontal resolution of BE than of FG in improving the TC analysis and prediction in a weak TC. Notably, the initial-TS case shows a greater nonlinear impact of the initial intensity on the intensity forecasts than the initial-hurricane case (cf. Figs. 11c and 11a). In contrast, for the increase of vertical resolution (Figs. 11b,d) in DA and forecasts,

TABLE 3. Error magnitudes of the TC initial (“Ana”) and strongest (“Peak”) maximum surface wind (MSW) during the forecasts in all experiments normalized by those in BASE for each case.

|                   |      | Horizontal       |                  |                  |              | Vertical         |                  |                  |           |
|-------------------|------|------------------|------------------|------------------|--------------|------------------|------------------|------------------|-----------|
|                   |      | FG(Hh)<br>BE(Hh) | FG(Hh)<br>BE(Lh) | FG(Lh)<br>BE(Hh) | BASE<br>(Hh) | FG(Hv)<br>BE(Hv) | FG(Hv)<br>BE(Lv) | FG(Lv)<br>BE(Hv) | BASE (Hv) |
| Initial-hurricane | Ana  | 0.5              | 0.25             | 0.31             | 1.0          | 0.26             | 0.06             | 0.56             | 1.0       |
|                   | Peak | 0.47             | 0.37             | 0.72             | 0.68         | 0.9              | 1.2              | 1.08             | 1.325     |
| Initial-TS        | Ana  | 0.33             | 1.25             | 0.25             | 1.0          | 0.26             | 0.83             | 0.42             | 1.0       |
|                   | Peak | 1.19             | 0.42             | 0.08             | 0.23         | 1.04             | 0.96             | 1.23             | 1.35      |

although the analyzed TC intensity becomes more accurate than BASE(Hv) or the most accurate [e.g., FG(Hv)BE(Lv) in the initial-hurricane case] among all the experiments (see Table 3), they only show little or no improvements to the intensity forecasts in Figs. 11b and 11d. The peak TC intensity forecast in the initial-hurricane case is weaker than in the initial-TS case, possibly due to the latter allowing a longer time for the model to spin up and intensify the vortex.

The forecasts of the midlevel ( $\sim 700$  hPa) and surface wind amplitudes near the eyewall valid at 0600 UTC 23 October were further verified against the flight-level and SFMR observations, respectively, for all experiments (Fig. 12). This verification is consistent with the intensity forecast (Fig. 11) in that increasing the horizontal resolution in free forecasts provides stronger and more accurate eyewall wind than increasing the vertical resolution (cf. solid and dashed lines with the same color). As in Fig. 11, the best forecast of the eyewall wind structure and intensity is achieved by increasing solely the FG horizontal resolution (FG(Hh)BE(Lh); orange solid line) in the initial-hurricane case, slightly better than FG(Hh)BE(Hh), while by increasing the BE horizontal resolution (FG(Lh)BE(Hh); green solid line) in the initial-TS case. The eyewall sizes in all forecasts are still overestimated even with a 1-km resolution model possibly due to the model deficiency for simulating extraordinarily small-size hurricanes like Patricia. The initial-TS case shows a larger variability of eyewall size than the initial-hurricane case due to the lost predictability at a longer lead time.

#### c. Impact of increased model resolution on TC structure prediction

This section diagnoses and interprets the mechanism of the impact of the improved TC analyses on subsequent intensity forecasts in terms of the TC structure evolutions. Three typical experiments in the initial-hurricane case were selected, including BASE(Hh), FG(Lh)BE(Hh), and FG(Hh)BE(Lh) with the same horizontal resolution in free forecasts but different initial conditions. FG(Lh)BE(Hh) and FG(Hh)BE(Lh) have improved the initial TC intensity and structure compared to BASE(Hh) by increasing solely the horizontal resolution of BE or FG, reaching similar accuracy of analyzed TC intensity (see Table 3). However, the former shows no change of intensity forecasts, while the latter shows apparent improvements of TC intensity and structure forecasts like FG(Hh)BE(Hh) (see Fig. 11a). The experiments in the initial-TS case are not studied because the stronger nonlinear process complicates the interpretation of the results.

As the assimilation of TCI dropsonde wind observations directly impacts the TC circulation in the analysis, especially near the eyewall, Fig. 13 shows the azimuthally averaged secondary circulation in the analysis and subsequent 18-h forecasts. At the initial time, the secondary circulation (zero vertical velocity in HWRF analyses) reveals the inflow at lower levels converging in the eyewall ( $\sim 30$  km; blue curves) and the upper-level outflow maximizing at around 60-km radius at 150 hPa. FG(Hh)BE(Lh) shows an evidently stronger inflow and outflow than the other two (cf. Fig. 13i vs Figs. 13a,e), favorable for more intense development of the secondary circulation. In contrast, FG(Lh)BE(Hh), despite the stronger initial MSW than BASE(Hh) (see Fig. 3a), shows a similar inflow strength with the maximum of nearly  $8 \text{ m s}^{-1}$  and a  $3 \text{ m s}^{-1}$  weaker outflow. It further signifies a smaller effect of increasing the BE resolution than increasing the FG resolution on the overall TC structure and intensity for an intense TC. At the 6-h lead time, the secondary circulation in the three experiments further intensifies with the eyewall (blue lines) shrunk to be closer to the TC center ( $\sim 15$  km). Noticeably, the initially stronger structure of coherent outflow and inflow in FG(Hh)BE(Lh) leads to its stronger TC secondary circulation than the other two at 6 h, especially the more intense and wider updraft near the eyewall (Fig. 13j). FG(Hh)BE(Lh) also shows the strongest downdraft originated from upper levels cascaded down the inner edge of the eyewall and turned to an outflow at low levels (cf. Fig. 11j vs Figs. 11b,f), possibly contributing to a more efficient adiabatic inner-core warming (Zhang and Chen 2012).

The stronger secondary circulation in FG(Hh)BE(Lh) maintains to the 18-h lead time when the peak intensity is reached. From 12 to 18 h, all the experiments present a weakening of the eyewall convection. Such weakening of the eyewall convection may be related to the gradual development of the concentric convection at the 40–50-km radius, possibly signifying the subsequent decay of Patricia.

The updraft in the eyewall lifts warm and moist air near the sea surface to higher levels, resulting in the condensation and latent heat release near the eyewall that significantly contributes to the TC intensification via diabatic heating. Therefore, following the TC secondary circulation in Figs. 13 and 14a–i show the azimuthally averaged total condensate (shaded) and diabatic heating rate (contour) at 6-, 12-, and 18-h lead times for the three experiments. Figures 14j–o show the differences of FG(Lh)BE(Hh) and FG(Hh)BE(Lh) from BASE(Hh). The concentrated total condensate (shaded) is primarily located

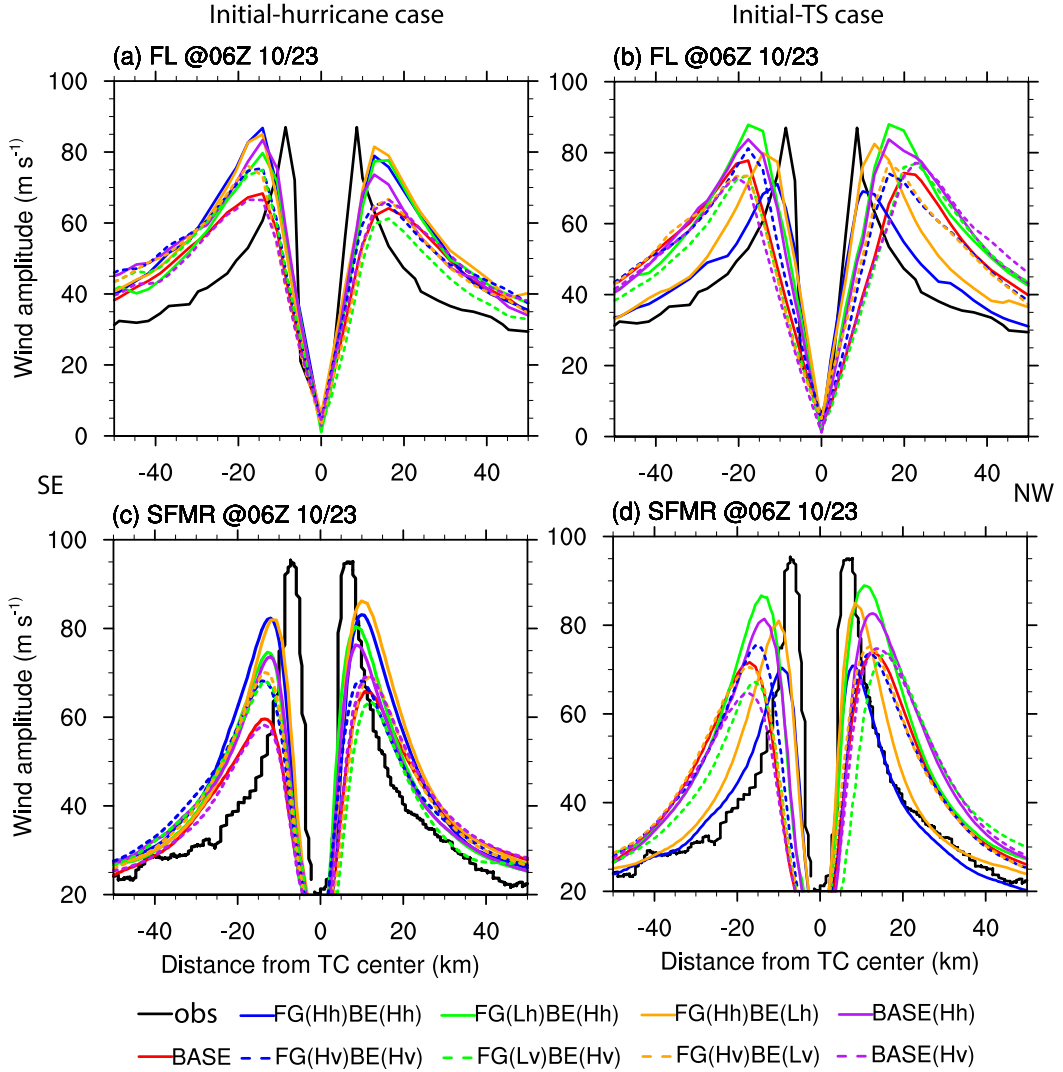


FIG. 12. (a) The midlevel ( $\sim 700$  hPa) and (c) surface wind speed in the forecasts valid at 0600 UTC 23 Oct in the initial-hurricane case verified against the flight-level and SFMR observations (black solid lines), respectively. (b),(d) As in (a) and (c), respectively, but for the initial-TS case.

above the freezing level ( $\sim 500$  hPa) in the eyewall, maximizing at around 300 hPa where the eyewall convection maximizes (Fig. 13). The intense diabatic heating rate (contours) shifted slightly inward to the inner edge of RMW (green lines) relative to the total condensate, matching the position of the deep updraft (cf. Figs. 14 and 13). Associated with the strength of eyewall convection (Fig. 13), FG(Hh)BE(Lh) presents a higher diabatic heating rate than BASE(Hh) in the eyewall (green lines) from 6 to 18 h (Figs. 14m–o), indicating a stronger TC intensification. In contrast, FG(Lh)BE(Hh) displays almost no difference of the diabatic heating rate relative to BASE(Hh) during the same period (Figs. 14j–l). FG(Hh)BE(Lh) also presents more intense total condensate than BASE(Hh) and FG(Lh)BE(Hh) near the upper-level outer edge of the eyewall at the 6- and 12-h lead times (cf. Figs. 14m,n and 14j,k). This result may be related to the stronger secondary

circulation in FG(Hh)BE(Lh) (Fig. 13) that causes more condensate droplets concentrated at upper levels and transported outwards in the outflow compared to FG(Lh)BE(Hh) and BASE(Hh). At the 18-h lead time, all the three experiments exhibit slightly reduced total condensate in the eyewall, possibly reaching the saturation of the generation and drop of condensate. These experiments thereby present much less differences of the total condensate compared to previous lead times.

The WB-57 aircraft flew across the core of Patricia during its mission on 22 October, collecting the unprecedented TCI dropsonde observations that provided an extraordinarily valuable whole-depth sampling of the thermodynamic structure within the warm core. Figure 15 shows the azimuthally averaged perturbation temperature ( $T'$ ) and relative humidity (RH) from the initial analysis time to 18-h lead time as well as

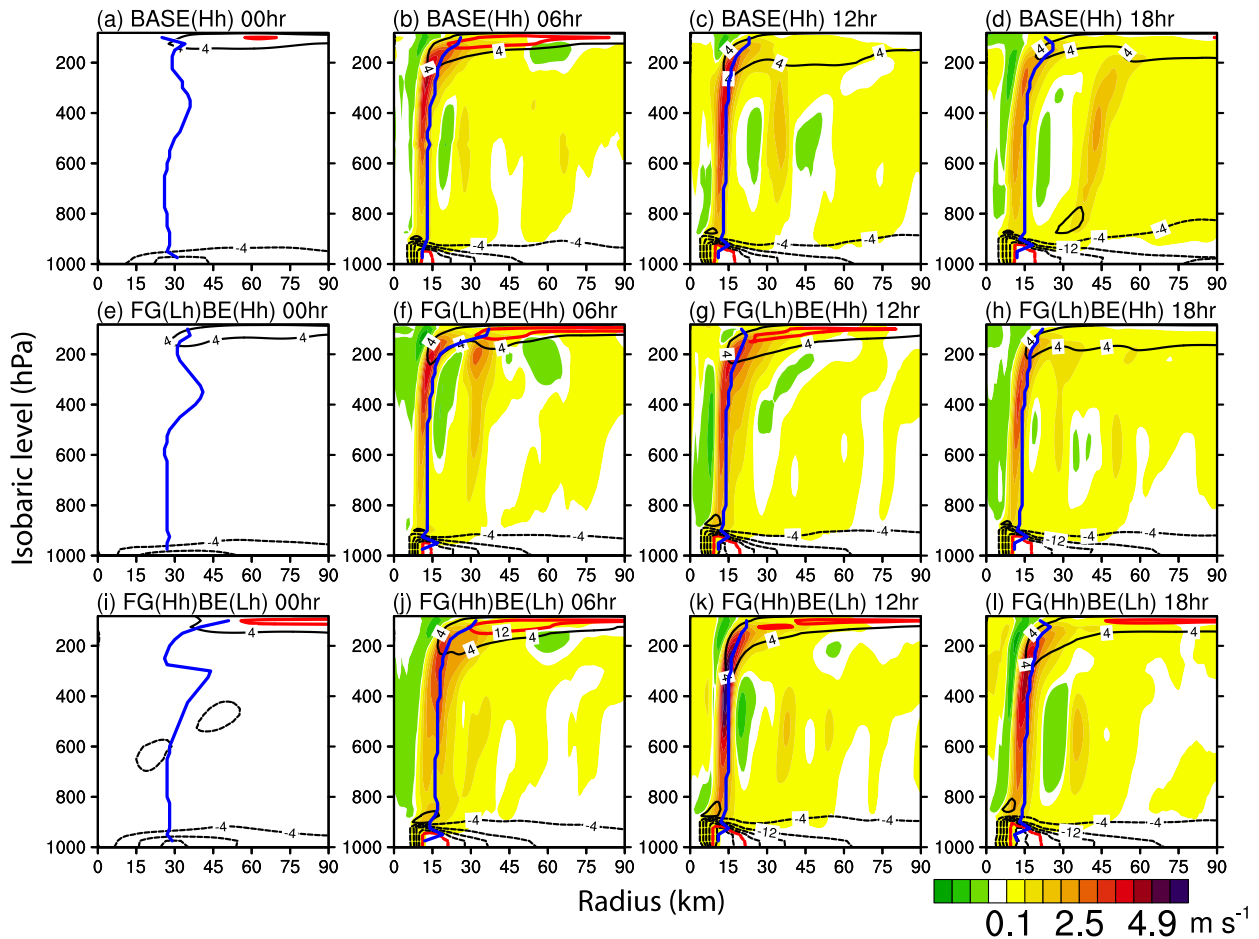


FIG. 13. The azimuthally averaged vertical (shaded) and radial (contours) winds ( $\text{m s}^{-1}$ ) of BASE in the initial-hurricane case at the (a) 0-, (b) 6-, (c) 12-, and (d) 18-h lead times. (e)–(h), (i)–(l) As in (a)–(d), but for FG(Lh)BE(Hh) and FG(Hh)BE(Lh), respectively. Red thick contours represent inflow of  $36 \text{ m s}^{-1}$  and outflow of  $12 \text{ m s}^{-1}$ . Blue lines denote the RMW.

the differences.  $T'$  is defined by removing the Jordan annual mean temperature (Jordan 1958) as was used in Rogers et al. (2017). At the initial time, the assimilation of the TCI dropsonde thermodynamic observations achieves an accurate depiction of the altitude (250–300 hPa) of the maximum inner-core  $T'$  for all the three experiments compared to Fig. 18a in Rogers et al. (2017). However, FG(Hh)BE(Lh) presents the most accurate maximum magnitude (14.75 K), followed by FG(Lh)BE(Hh) (14.06 K) and BASE(Hh) (13.29 K) as the observation is 14.9 K (Rogers et al. 2017). This is mainly due to the more accurate AI of the inner-core temperature in FG(Hh)BE(Lh) as a result of the better-resolved FG of temperature (see Figs. 8e,f). In addition to the maximum temperature, FG(Hh)BE(Lh) presents an overall warmer inner core than BASE(Hh) in the analysis (Fig. 15q), especially at the mid- and high levels above 600 hPa and the low levels below 800 hPa. Their differences are much larger than those between FG(Lh)BE(Hh) and BASE(Hh) (Fig. 15m). It indicates that increasing the FG horizontal resolution is more effective than increasing the BE horizontal resolution in improving not only the TC vortex circulation but also the

warm-core structure in the analyses for the initial-hurricane case. Despite the assimilation of moisture observations, none of the experiments can offer a realistic RH structure, especially the dry inner core (Figs. 15a,e,i).

The inner-core  $T'$  gradually increases during the following 18 h, tied to the formation and intensification of the drier warm core. The warm-core difference between FG(Hh)BE(Lh) and BASE(Hh) at 6 h becomes much weaker than at the initial time (cf. Figs. 15r and 15q). Nevertheless, FG(Hh)BE(Lh) remains the warmer (shaded) and drier (contour) inner core than BASE(Hh) through the 18-h lead time (Figs. 15r–t), which is consistent with the intensity forecasts (Fig. 11a). In contrast, FG(Lh)BE(Hh) presents only slight differences of  $T'$  and RH in the warm core from BASE(Hh) (cf. Figs. 15n–p and 15j–l). Beyond the eyewall (red line), the three experiments show very little difference.

## 5. Conclusions and discussion

Previous studies have demonstrated that increasing the horizontal or vertical resolution of free forecast models can

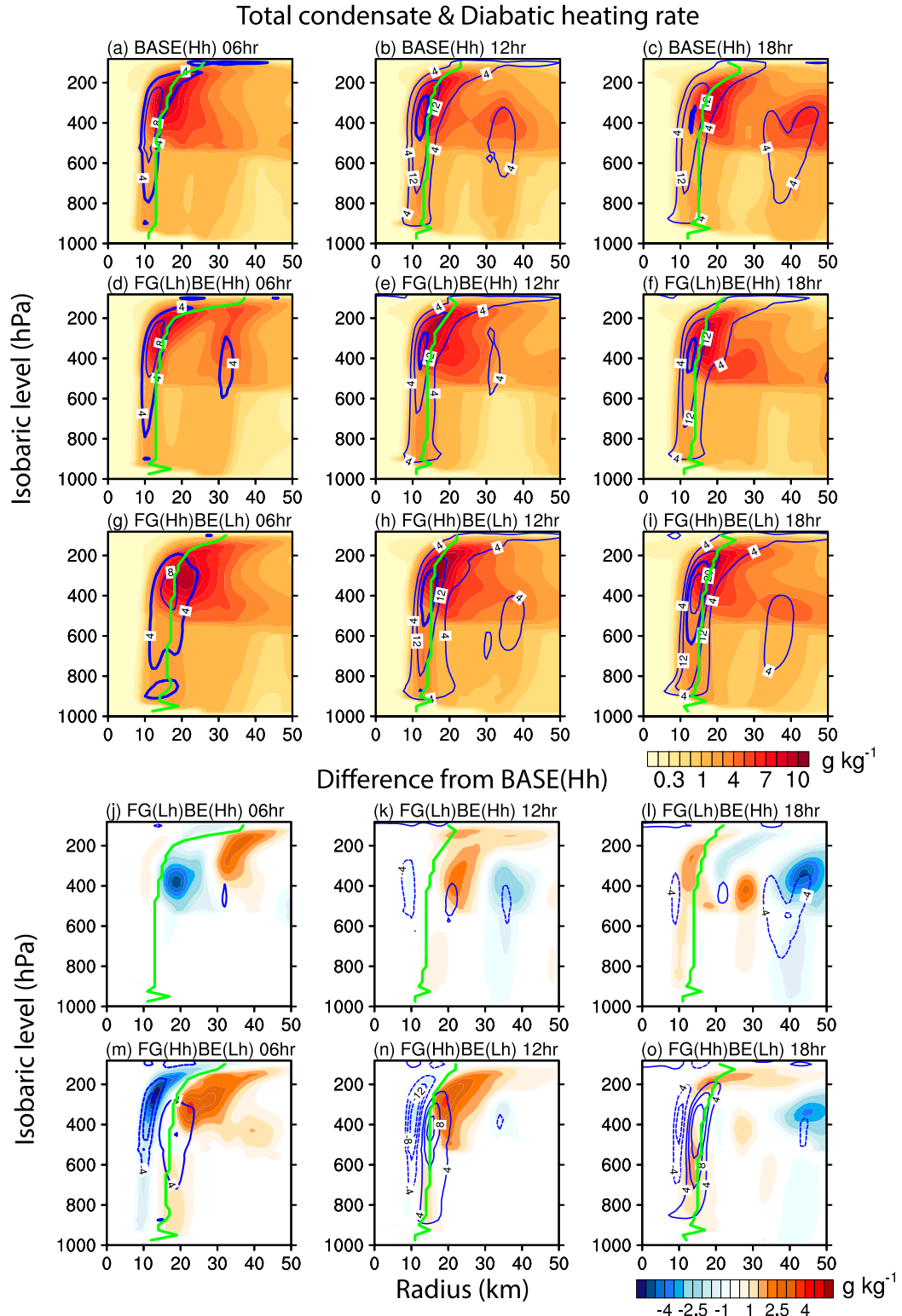


FIG. 14. (a)–(i) As in Fig. 13, but for the total condensate (shaded; unit:  $\text{g kg}^{-1}$ ) and diabatic heating rate (contours; unit:  $10^{-3} \text{ K s}^{-1}$ ). Blue thick contours represent diabatic heating rate of  $4 \times 10^{-3} \text{ K s}^{-1}$  in (a), (d), and (g) and  $20 \times 10^{-3} \text{ K s}^{-1}$  in (b), (c), (e), (f), (h), and (i). (j)–(o) The differences of FG(Lh)BE(Hh) and FG(Hh)BE(Lh) from BASE(Hh). Green lines denote the RMW.

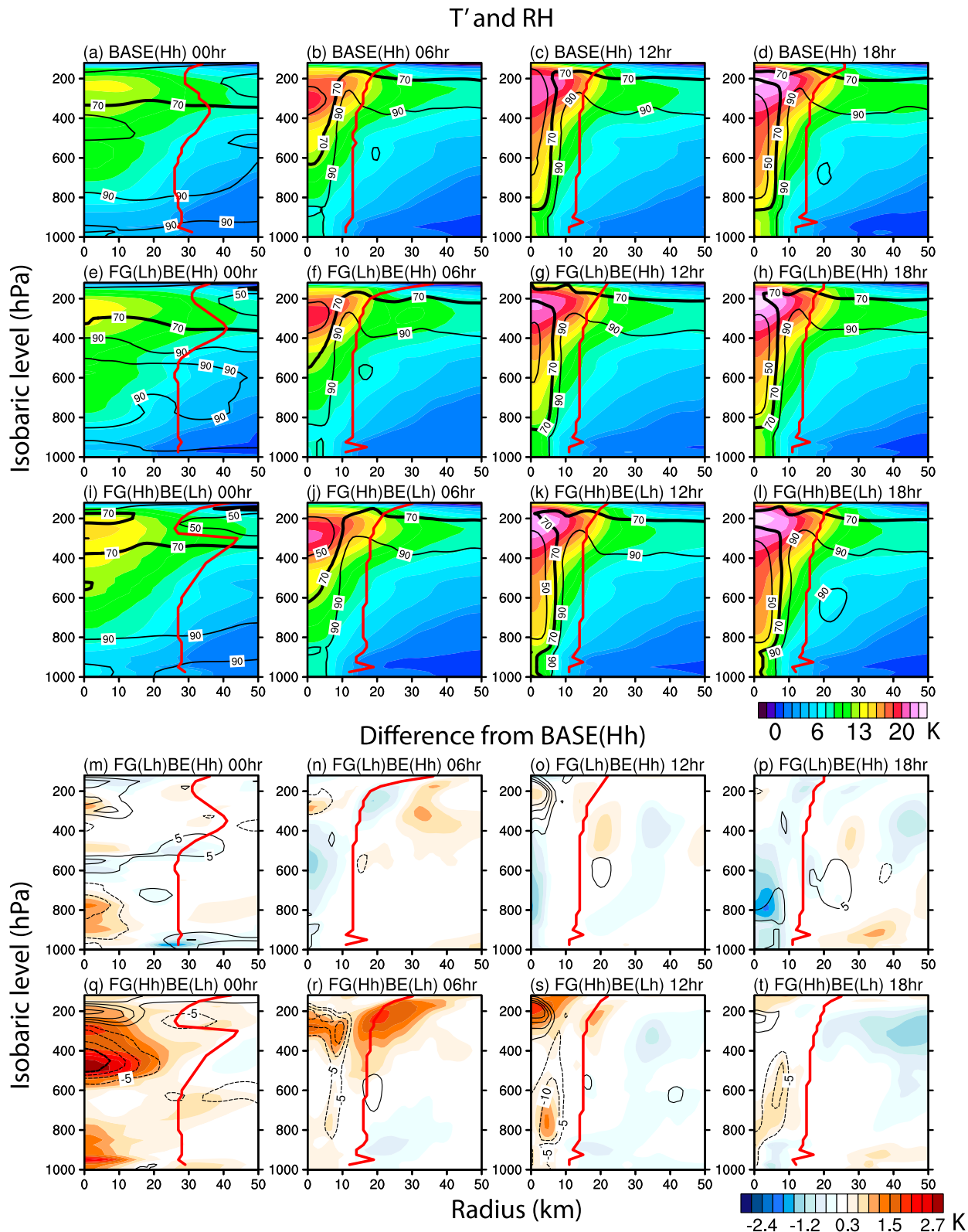


FIG. 15. As in Fig. 14, but for perturbation temperature (shaded; unit: K) and relative humidity (RH; contours; %). Black thick contours in (a)–(l) represent RH of 70%. Red lines denote the RMW.

improve TC intensity and structure forecasts to some extent. In almost all of these studies, the analyses were directly interpolated to an increased resolution to initialize the high-resolution forecasts. It is still poorly understood if and how the increased model resolution within the data assimilation will impact the analyses and subsequent forecasts of the TC intensity and structure.

This study investigated the impact of the increased resolution during DA on the TC analyses and subsequent forecasts using the hybrid EnVar system for HWRF. The EnVar DA system uses a single short-range forecast as the FG (i.e., first guess) state and a group of short-range BE (i.e., background ensemble) forecasts to estimate the background error covariance. Therefore, the impact of increasing the resolution of FG and BE were studied separately. In addition, this study investigated the individual impact of increasing the horizontal and vertical model resolution during DA, which was not studied previously. A particular event, hurricane Patricia in 2015, was used in this paper because its extraordinarily small size and record-breaking strong intensity and rapid intensification rate resulted in a large underestimation of TC intensity in all operational forecasts. Despite being a single event, two typical cases during its lifetime were studied for comparison. These cases are initialized from a tropical storm (i.e., initial-TS case) and a hurricane (i.e., initial-hurricane case), respectively. The same observations, i.e., the high-definition and wide-ranging TCI dropsonde observations, were assimilated in all experiments so that other available observations can serve as a reference for verification.

In conclusion, the main results relating to the error magnitudes of the TC initial and forecasted peak MSW (i.e., maximum surface wind) in all experiments are summarized in Table 3. The major conclusions include:

- 1) Impact of FG versus BE resolution on TC analyses in the initial-hurricane case. In the initial-hurricane case, increasing the FG resolution is more effective than increasing the BE resolution in improving the analyzed TC intensity and structure. The improved FG contributes to a better TC analysis directly through the more accurate simulation of the TC intensity and structure in the background, especially the finescale features near the eyewall, or through the reduced observational innovation in DA.
- 2) Impact of FG versus BE resolution on TC analyses in the initial-TS case. In the initial-TS case, different from the initial-hurricane case, increasing the FG resolution shows little or no improvement to the analyzed TC intensity. In contrast, increasing the BE resolution is more effective than increasing the FG resolution in improving TC analyses. Such effect is attributed to the better finescale background spatial correlation estimated from a higher-resolution BE that improves the extrapolation of the observational innovation.
- 3) Increasing horizontal versus vertical resolution on TC analyses. In the initial-hurricane case, increasing horizontal resolution in either FG or BE produces a significantly stronger TC analysis than increasing vertical resolution (Fig. 3). Meanwhile, increasing solely the FG horizontal

resolution [i.e., FG(Hh)BE(Lh)] produces the most accurate initial maximum warm core and the second-best accurate analyzed MSW. In the initial-TS case, the relative importance between the increase of horizontal and vertical resolution is mixed. The increase of FG resolution slightly improves the TC sizes in analyses for the initial-hurricane case.

- 4) Impact of increasing horizontal versus vertical resolution during the free forecasts. In both initial-hurricane and initial-TS cases, increasing the horizontal resolution in free forecasts significantly improves the forecast of peak MSW compared to BASE. However, all the experiments increasing the vertical resolution during free forecasts have almost no improvement of the TC peak intensity forecast compared to BASE.
- 5) Impact of improved TC analyses on intensity forecasts. Intensity forecasts in both initial-hurricane and initial-TS cases suggest that more accurate TC intensity and structure in the analysis as a result of increased resolution during DA can improve the intensity prediction. In the initial-hurricane case, FG(Hh)BE(Lh) that increases solely the FG horizontal resolution in DA presents the most accurate peak MSW forecast. Diagnostics suggest this is attributed to the much-amplified inflow and outflow in the analysis of FG(Hh)BE(Lh), resulting in the more intense updraft and condensation in the eyewall that releases more diabatic heating to intensify the TC. In the initial-TS case, the positive impact of improved analysis extends to an even longer lead time, though the impact is more nonlinear than in the initial-hurricane case.

Our study uses a particular case, Patricia, which has extraordinarily small size and strong intensity and intensification rate. Moreover, the high-fidelity and high-density TCI dropsonde observations used here may not be available for other cases. Therefore, caution needs to be taken when generalizing the conclusions to other cases, especially some weaker and less organized TC cases. Nevertheless, this study does offer a new avenue to potentially overcome the underestimation of TC intensity in analysis and prediction. More importantly, our study revealed both from the DA and dynamics point of view how the FG and BE with increased resolution impact the TC analyzed intensity and structure and the subsequent forecasts. Compared to most of existing studies that simply interpolated initial conditions to initialize higher-resolution free forecasts, using higher-resolution FG or BE during DA may provide more accurate initial conditions and thus may lead to additional improvement in TC forecasts as illustrated in our results. Similar studies should be further extended to more cases and TC phases in the future to examine the generality of the conclusions from this study. In addition, the impact of increasing model resolution during DA should be further examined when other utilities (e.g., vortex modification) are adopted.

**Acknowledgments.** The research documented in this paper is supported by the ONR Grants N00014-14-1-0125 and N000141712111 and NOAA Grants NA14NWS4680021 and NA16NWS4680028. We thank TCI PIs James Doyle and

Michael Bell for providing the TCI HDSS dropsonde data and Christopher Velden for providing the AMV observations. We are also grateful to the IFEX program for providing the SFMR, FL, and TDR observations. We acknowledge Dr. Aaron Johnson for proofreading the manuscript.

**Data availability statement.** All model data produced during this study has been archived locally and is available upon request to the corresponding author.

## REFERENCES

- Alpert, J. C., and V. K. Kumar, 2007: Radial wind super-obs from the WSR-88D radars in the NCEP operational assimilation system. *Mon. Wea. Rev.*, **135**, 1090–1109, <https://doi.org/10.1175/MWR3324.1>.
- Bell, M. M., and Coauthors, 2016: ONR tropical cyclone intensity 2015 NASA WB-57 HDSS dropsonde data, version 1.0. UCAR/NCAR–Earth Observatory Laboratory, accessed 1 May 2016, <https://doi.org/10.5065/D6KW5D8M>.
- Biswas, M. K., and Coauthors, 2018: Hurricane Weather Research and Forecasting (HWRF) model: 2018 scientific documentation. Developmental Testbed Center, 112 pp., [http://www.dtcenter.org/sites/default/files/community-code/hwrf/docs/scientific\\_documents/HWRFv4.0a\\_ScientificDoc.pdf](http://www.dtcenter.org/sites/default/files/community-code/hwrf/docs/scientific_documents/HWRFv4.0a_ScientificDoc.pdf).
- Black, P. G., L. Harrison, M. Beaubien, R. Bluth, H. Jonsson, A. B. Penny, R. W. Smith, and J. D. Doyle, 2017: High Definition Sounding System (HDSS) for atmospheric profiling. *J. Atmos. Oceanic Technol.*, **34**, 777–796, <https://doi.org/10.1175/JTECH-D-14-00210.1>.
- Chen, S. S., J. F. Price, W. Zhao, M. A. Donelan, and E. J. Walsh, 2007: The CBLAST-Hurricane Program and the next-generation fully coupled atmosphere–wave–ocean models for hurricane research and prediction. *Bull. Amer. Meteor. Soc.*, **88**, 311–318, <https://doi.org/10.1175/BAMS-88-3-311>.
- Christophersen, H., A. Aksoy, J. Dunion, and K. Sellwood, 2017: The impact of NASA Global Hawk unmanned aircraft dropwindsonde observations on tropical cyclone track, intensity, and structure: Case studies. *Mon. Wea. Rev.*, **145**, 1817–1830, <https://doi.org/10.1175/MWR-D-16-0332.1>.
- Davis, C., W. Wang, J. Dudhia, and R. Torn, 2010: Does increased horizontal resolution improve hurricane wind forecasts? *Wea. Forecasting*, **25**, 1826–1841, <https://doi.org/10.1175/2010WAF2222423.1>.
- DeMaria, M., C. R. Sampson, J. A. Knaff, and K. D. Musgrave, 2014: Is tropical cyclone intensity guidance improving? *Bull. Amer. Meteor. Soc.*, **95**, 387–398, <https://doi.org/10.1175/BAMS-D-12-00240.1>.
- Doyle, J. D., and Coauthors, 2017: A view of tropical cyclones from above: The Tropical Cyclone Intensity (TCI) experiment. *Bull. Amer. Meteor. Soc.*, **98**, 2113–2134, <https://doi.org/10.1175/BAMS-D-16-0055.1>.
- Feng, J., and X. G. Wang, 2019: Impact of assimilating upper-level dropsonde observations collected during the TCI field campaign on the prediction of intensity and structure of Hurricane Patricia (2015). *Mon. Wea. Rev.*, **147**, 3069–3089, <https://doi.org/10.1175/MWR-D-18-0305.1>.
- Franklin, J. L., J. Kaplan, C. S. Velden, and C. M. Hayden, 1990: Some comparisons of VAS and dropwindsonde data over the subtropical Atlantic. *Mon. Wea. Rev.*, **118**, 1869–1887, [https://doi.org/10.1175/1520-0493\(1990\)118<1869:SCOVAD>2.0.CO;2](https://doi.org/10.1175/1520-0493(1990)118<1869:SCOVAD>2.0.CO;2).
- Gopalakrishnan, S. G., and Coauthors, 2010: Hurricane Weather Research and Forecasting (HWRF) model scientific documentation. Development Testbed Center, 80 pp., [http://photino.cwb.gov.tw/rdcweb/lib/brief/201106-27-28\\_HWRF\\_HWRF\\_final\\_2-2\\_cm.pdf](http://photino.cwb.gov.tw/rdcweb/lib/brief/201106-27-28_HWRF_HWRF_final_2-2_cm.pdf).
- , S. Goldenberg, T. Quirino, X. Zhang, F. D. Marks Jr., K.-S. Yeh, R. Atlas, and V. Tallapragada, 2012: Toward improving high-resolution numerical hurricane forecasting: Influence of model horizontal grid resolution, initialization, and physics. *Wea. Forecasting*, **27**, 647–666, <https://doi.org/10.1175/WAF-D-11-00055.1>.
- Han, J., and H.-L. Pan, 2006: Sensitivity of hurricane intensity forecasts to convective momentum transport parameterization. *Mon. Wea. Rev.*, **134**, 664–674, <https://doi.org/10.1175/MWR3090.1>.
- Harnos, D. S., and S. W. Nesbitt, 2011: Convective structure in rapidly intensifying tropical cyclones as depicted by passive microwave measurements. *Geophys. Res. Lett.*, **38**, L07805, <https://doi.org/10.1029/2011GL047010>.
- Houtekamer, P. L., H. L. Mitchell, G. Pellerin, M. Buehner, M. Charron, L. Spacek, and B. Hansen, 2005: Atmospheric data assimilation with an ensemble Kalman filter: Results with real observations. *Mon. Wea. Rev.*, **133**, 604–620, <https://doi.org/10.1175/MWR-2864.1>.
- HRD, 2015: Hurricane Research Division dataset during Hurricane Patricia. NOAA, accessed 19 November 2017, [http://www.aoml.noaa.gov/hrd/Storm\\_pages/patricia2015/](http://www.aoml.noaa.gov/hrd/Storm_pages/patricia2015/).
- Jordan, C. L., 1958: Mean soundings for the West Indies area. *J. Meteor.*, **15**, 91–97, [https://doi.org/10.1175/1520-0469\(1958\)015<0091:MSFTWI>2.0.CO;2](https://doi.org/10.1175/1520-0469(1958)015<0091:MSFTWI>2.0.CO;2).
- Katz, R. W., and A. H. Murphy, 2015: *Economic Value of Weather and Climate Forecasts*. Cambridge University Press, 240 pp.
- Kimball, S. K., and F. C. Dougherty, 2006: The sensitivity of idealized hurricane structure and development to the distribution of vertical levels in MM5. *Mon. Wea. Rev.*, **134**, 1987–2008, <https://doi.org/10.1175/MWR3171.1>.
- Knapp, K. R., M. C. Kruk, D. H. Levinson, H. J. Diamond, and C. J. Neumann, 2010: The International Best Track Archive for Climate Stewardship (IBTrACS): Unifying tropical cyclone data. *Bull. Amer. Meteor. Soc.*, **91**, 363–376, <https://doi.org/10.1175/2009BAMS2755.1>.
- Li, Y., X. Wang, and M. Xue, 2012: Assimilation of radar radial velocity data with the WRF ensemble-3DVAR hybrid system for the prediction of hurricane Ike (2008). *Mon. Wea. Rev.*, **140**, 3507–3524, <https://doi.org/10.1175/MWR-D-12-00043.1>.
- Liu, Q., N. Surgi, S. Lord, W. S. Wu, D. Parrish, S. Gopalakrishnan, J. Waldrop, and J. Gamache, 2006: Hurricane initialization in HWRF model. *27th Conf. on Hurricanes and Tropical Meteorology*, Monterey, CA, Amer. Meteor. Soc., 8A.2, [http://ams.confex.com/ams/27Hurricanes/techprogram/paper\\_108496.htm](http://ams.confex.com/ams/27Hurricanes/techprogram/paper_108496.htm).
- Lu, X., and X. Wang, 2019: Improving hurricane analyses and predictions with TCI, IFEX field campaign observations, and CIMSS AMVs using the advanced hybrid data assimilation system for HWRF. Part I: What is missing to capture the rapid intensification of Hurricane Patricia (2015). *Mon. Wea. Rev.*, **147**, 1351–1373, <https://doi.org/10.1175/MWR-D-18-0202.1>.
- , and —, 2020: Improving hurricane analyses and predictions with TCI, IFEX field campaign observations, and CIMSS AMVs using the advanced hybrid data assimilation system for HWRF. Part II: Observation impacts on the analysis and prediction of Patricia (2015). *Mon. Wea. Rev.*, **148**, 1407–1430, <https://doi.org/10.1175/MWR-D-19-0075.1>.

- , —, Y. Li, M. Tong, and X. Ma, 2017a: GSI-based ensemble-variational hybrid data assimilation for HWRF for hurricane initialization and prediction: Impact of various error covariances for airborne radar observation assimilation. *Quart. J. Roy. Meteor. Soc.*, **143**, 223–239, <https://doi.org/10.1002/qj.2914>.
- , —, M. Tong, and V. Tallapragada, 2017b: GSI-based, continuously cycled, dual-resolution hybrid ensemble-variational data assimilation system for HWRF: System description and experiments with Edouard (2014). *Mon. Wea. Rev.*, **145**, 4877–4898, <https://doi.org/10.1175/MWR-D-17-0068.1>.
- Mehra, A., V. Tallapragada, Z. Zhang, B. Liu, L. Zhu, W. Wang, and H.-S. Kim, 2018: Advancing the state of the art in operational tropical cyclone forecasting at NCEP. *Trop. Cyclone Res. Rev.*, **7**, 51–56, <https://doi.org/10.6057/2018TCRR01.06>.
- Nystrom, R. G., and F. Zhang, 2019: Practical uncertainties in the limited predictability of the record-breaking intensification of Hurricane Patricia (2015). *Mon. Wea. Rev.*, **147**, 3535–3556, <https://doi.org/10.1175/MWR-D-18-0450.1>.
- Poteat, K. O., 1973: A comparison of satellite-derived, low-level and cirrus-level winds with conventional wind observations. *J. Appl. Meteor.*, **12**, 1416–1419, [https://doi.org/10.1175/1520-0450\(1973\)012<1417:ACOSDL>2.0.CO;2](https://doi.org/10.1175/1520-0450(1973)012<1417:ACOSDL>2.0.CO;2).
- Pu, Z., X. Li, and J. Sun, 2009: Impact of airborne Doppler radar data assimilation on the numerical simulation of intensity changes of Hurricane Dennis near a landfall. *J. Atmos. Sci.*, **66**, 3351–3365, <https://doi.org/10.1175/2009JAS3121.1>.
- , S. Zhang, M. Tong, and V. Tallapragada, 2016: Influence of the self-consistent regional ensemble background error covariance on hurricane inner-core data assimilation with the GSI-based hybrid system for HWRF. *J. Atmos. Sci.*, **73**, 4911–4925, <https://doi.org/10.1175/JAS-D-16-0017.1>.
- Qin, N., and D.-L. Zhang, 2018: On the extraordinary intensification of Hurricane Patricia (2015). Part I: Numerical experiments. *Wea. Forecasting*, **33**, 1205–1224, <https://doi.org/10.1175/WAF-D-18-0045.1>.
- Rogers, R., and Coauthors, 2006: The Intensity Forecasting Experiment: A NOAA multiyear field program for improving tropical cyclone intensity forecasts. *Bull. Amer. Meteor. Soc.*, **87**, 1523–1538, <https://doi.org/10.1175/BAMS-87-11-1523>.
- , and Coauthors, 2017: Rewriting the tropical record books: The extraordinary intensification of Hurricane Patricia (2015). *Bull. Amer. Meteor. Soc.*, **98**, 2091–2112, <https://doi.org/10.1175/BAMS-D-16-0039.1>.
- Schwartz, C. S., 2016: Improving large-domain convection-allowing forecasts with high-resolution analyses and ensemble data assimilation. *Mon. Wea. Rev.*, **144**, 1777–1803, <https://doi.org/10.1175/MWR-D-15-0286.1>.
- Sears, J., and C. S. Velden, 2012: Validation of satellite-derived atmospheric motion vectors and analyses around tropical disturbances. *J. Appl. Meteor. Climatol.*, **51**, 1823–1834, <https://doi.org/10.1175/JAMC-D-12-024.1>.
- Sippel, J. A., F. Zhang, Y. Weng, L. Tian, G. M. Heymsfield, and S. A. Braun, 2014: Ensemble Kalman filter assimilation of HIWRAP observations of Hurricane Karl (2010) from the unmanned Global Hawk aircraft. *Mon. Wea. Rev.*, **142**, 4559–4580, <https://doi.org/10.1175/MWR-D-14-00042.1>.
- Smith, R. K., M. T. Montgomery, and N. Van Sang, 2009: Tropical cyclone spin-up revisited. *Quart. J. Roy. Meteor. Soc.*, **135**, 1321–1335, <https://doi.org/10.1002/qj.428>.
- Tallapragada, V., and Coauthors, 2016: Hurricane Weather Research and Forecasting (HWRF) model: 2015 scientific documentation. NCAR Tech. Note NCAR/TN-522+STR, 122 pp., <https://doi.org/10.5065/D6ZP44B5>.
- Tong, M., and Coauthors, 2018: Impact of assimilating aircraft reconnaissance observations on tropical cyclone initialization and prediction using operational HWRF and GSI ensemble-variational hybrid data assimilation. *Mon. Wea. Rev.*, **146**, 4155–4177, <https://doi.org/10.1175/MWR-D-17-0380.1>.
- Wang, X., 2010: Incorporating ensemble covariance in the Gridpoint Statistical Interpolation (GSI) variational minimization: A mathematical framework. *Mon. Wea. Rev.*, **138**, 2990–2995, <https://doi.org/10.1175/2010MWR3245.1>.
- , and C. H. Bishop, 2003: A comparison of breeding and ensemble transform Kalman filter ensemble forecast schemes. *J. Atmos. Sci.*, **60**, 1140–1158, [https://doi.org/10.1175/1520-0469\(2003\)060<1140:ACOBAE>2.0.CO;2](https://doi.org/10.1175/1520-0469(2003)060<1140:ACOBAE>2.0.CO;2).
- , D. Parrish, D. Kleist, and J. S. Whitaker, 2013: GSI 3DVar-based ensemble-variational hybrid data assimilation for NCEP global forecast system: Single resolution experiments. *Mon. Wea. Rev.*, **141**, 4098–4117, <https://doi.org/10.1175/MWR-D-12-00141.1>.
- Weng, Y., and F. Zhang, 2012: Assimilating airborne Doppler radar observations with an ensemble Kalman filter for convection-permitting hurricane initialization and prediction: Katrina (2005). *Mon. Wea. Rev.*, **140**, 841–859, <https://doi.org/10.1175/2011MWR3602.1>.
- Willoughby, H. E., 1990: Gradient balance in tropical cyclones. *J. Atmos. Sci.*, **47**, 265–274, [https://doi.org/10.1175/1520-0469\(1990\)047<0265:GBITC>2.0.CO;2](https://doi.org/10.1175/1520-0469(1990)047<0265:GBITC>2.0.CO;2).
- Zhang, B. L., R. S. Lindzen, V. Tallapragada, F. Weng, Q. Liu, J. A. Sippel, Z. Ma, and M. A. Bender, 2016: Increasing vertical resolution in U.S. models to improve track forecasts of Hurricane Joaquin with HWRF as an example. *Proc. Natl. Acad. Sci. USA*, **113**, 11 765–11 769, <https://doi.org/10.1073/pnas.1613800113>.
- Zhang, D. L., and X. Wang, 2003: Dependence of hurricane intensity and structures on vertical resolution and time-step size. *Adv. Atmos. Sci.*, **20**, 711–725, <https://doi.org/10.1007/BF02915397>.
- , and H. Chen, 2012: Importance of the upper-level warm core in the rapid intensification of a tropical cyclone. *Geophys. Res. Lett.*, **39**, L02806, <https://doi.org/10.1029/2011GL050578>.
- , L. Zhu, X. Zhang, and V. Tallapragada, 2015: Sensitivity of idealized hurricane intensity and structures under varying background flows and initial vortex intensities to different vertical resolutions in HWRF. *Mon. Wea. Rev.*, **143**, 914–932, <https://doi.org/10.1175/MWR-D-14-00102.1>.
- Zhang, F., and D. Tao, 2013: Effects of vertical wind shear on the predictability of tropical cyclones. *J. Atmos. Sci.*, **70**, 975–983, <https://doi.org/10.1175/JAS-D-12-0133.1>.
- , Y. Weng, J. A. Sippel, Z. Meng, and C. H. Bishop, 2009: Cloud-resolving hurricane initialization and prediction through assimilation of Doppler radar observations with an ensemble Kalman filter. *Mon. Wea. Rev.*, **137**, 2105–2125, <https://doi.org/10.1175/2009MWR2645.1>.
- Zhang, X., T. S. Quirino, S. Gopalakrishnan, K.-S. Yeh, F. D. Marks Jr., and S. B. Goldenberg, 2011: HWRFX: Improving hurricane forecasts with high resolution modeling. *Comput. Sci. Eng.*, **13**, 13–21, <https://doi.org/10.1109/MCSE.2010.121>.
- Zhu, P., B. Tyner, J. A. Zhang, E. Aligo, S. Gopalakrishnan, F. D. Marks, A. Mehra, and V. Tallapragada, 2019: Role of eyewall and rainband eddy forcing in tropical cyclone intensification. *Atmos. Chem. Phys.*, **19**, 14 289–14 310, <https://doi.org/10.5194/acp-19-14289-2019>.